Biomedical Therapy Delivery by Fluid-Mechanic Means

A Thesis
SUBMITTED TO THE FACULTY OF
UNIVERSITY OF MINNESOTA
BY

James Michael Weiler

IN PARTIAL FULFILLMENT OF THE REQUIREMENTS
FOR THE DEGREE OF
DOCTOR OF PHILOSOPHY

Professor Ephraim Sparrow, Advisor

January 2014

ACKNOWLEDGMENTS

This work benefited greatly from the help of many fellow students and staff. I first want to thank fellow graduate students Reza Ramazani, Dan Bettenhausen, and John Gorman. Your assistance throughout my efforts was always greatly appreciated.

While there are too many to list in totality, I want to thank some of my Professors for being part of my academic career. I appreciate the additional time required from your busy schedules to serve on my masters and/or doctoral committees and provide your valuable input. These Professors included Paul Strykowski, Sant Arora, Chris Hogan, Cari Dutcher, and James Ramsey.

This work would not have been possible without the tireless support from my advisor, Professor Ephraim Sparrow. My academic career, and life in total, have been truly blessed by having the opportunity to work with Professor Sparrow. His unrelenting work ethic, unquenchable thirst for new knowledge, and desire and patience to teach anyone willing to listen are without equal. The many lives of those he has worked with, the University of Minnesota, and the vast field of mechanical engineering are forever indebted to this wonderful and talented man – thank you.

I must also give my sincere thanks to my wonderful wife for giving me the time and space to chase this selfish goal. Her support allowed me to spend countless hours away from home while she held our home together and took care of our amazing kids. She never questioned my desire or motivation, but I know she sacrificed her personal time in order to support my efforts. I will never be able to thank you enough – I love you.

DEDICATION

The work done in preparation of, and documented in this thesis, is in dedication to my children. Let this be a reminder to you that with time, patience, and hard work, anything is possible. The world is there for you to take in as much as you desire. Furthering your education will enlighten you to new ideas and concepts that you may not have previously considered. This additional insight will give you a new perspective on life and make your star shine just a little brighter. I love each of you more than you will ever know.

ABSTRACT

The efficacy of many biomedical therapies can be improved when the physical processes which underlie the treatment modality are thoroughly understood. Many treatments make use of transport processes that are deeply embedded in mechanical engineering theory and practice. The research documented in this thesis is firmly based on fluid-mechanic, heat-transfer, mass-transfer, and particle transport theory. The thesis encompasses three categories of biomedical applications: drug distribution, thermal-based surgery, and drug delivery by means of particle transport.

The first application dealt with a drug-eluting stent and with the distribution of the drug both into the artery wall by diffusion as well as into the blood flowing in the lumen via advection. This conjugate problem was redefined in dimensionless form and solved by numerical simulation to yield universal solutions. The solutions revealed the existence of a mass transfer boundary layer adjacent to the surface of the stent. Upstream diffusion, opposite to the direction of the advection, occurred. The results showed that the mass transfer into the flowing blood was orders of magnitude larger than the diffusive transfer into the artery walls.

The focus of the second application was an in-depth, a fundamentals-based investigation of a new, minimally invasive treatment for menorrhagia. The involved physical processes include vapor transport into the uterine cavity, heat liberated by phase-change, and heat penetration into human tissue by means of conduction and blood perfusion. Cell necrosis was achieved by elevated temperatures sustained for a sufficient period of time. The outcome of this work was the depth of tissue necrosis corresponding to a given duration of the treatment. The predicted depths of necrosis compared favorably with clinical results.

The final focus was the creation of a new methodology for the accurate delivery to targeted sites of drug particulates administered either through the mouth or the nose. The drug particles are carried through the respiratory system by an air stream. A numerical-based solution process was developed utilizing the laws of fluid mechanics, the physics of particle transport, and impaction theory. The final solution proved capable of predicting the landing locations of particles based on their respective sizes.

Table of Contents

Contents **Page**

LIST OF TABLES

Table **Page**

LIST OF FIGURES

Figure **Page**

CHAPTER 1 – INTRODUCTION AND MOTIVATIONS

Many biomedical remedial devices can be studied and better understood by careful examination of the fundamental processes which drive the resultant therapy. Many of these processes are some of the basic phenomena studied and explored in the field of mechanical engineering. Biological functions such as respiration and the cardiovascular circulation system are defined by the transport processes of fluid dynamics. Similarly, the use and delivery of drugs within the body are profoundly related to mass transfer and fluid dynamics. Additionally there are various conditions and therapies that involve the transport of heat such as hyperthermia or hypothermia. Thermally based therapies have replaced traditional surgery in numerous instances. This brief review suggests a strong synergy between mechanical-engineering-based transport processes and biomedical functions and therapies.

The use of numerical simulation as a modality for the quantification of complex physical processes has enabled competent predictions of biomedical responses to therapeutic actions. Of special significance to this thesis is the heightened capability of software focused on fluid dynamics, heat transfer, mass transfer, and particle transport as they apply to mechanical engineering. The key to the successful use of that software is the art and science of modeling. Even with the increased capacity of computing equipment, total fidelity to real systems, especially those relevant to biological processes, is not yet possible.

The mathematical descriptions of all the physical processes that are relevant to this thesis encompass non-linear, simultaneous, partial differential equations. To the best knowledge of the author, only analogue computers are able to solve differential equations as such [1]. Digital computers are restricted to solving discretized forms of differential equations. Discretization is a process by which differential equations are metamorphized to algebraic equations. The three best-

known methods to accomplish this transformation are finite-difference, finite-element, and finite-volume. Of these, finite-element discretization is favored for structural analysis, finite-volume is favored for fluid mechanics, heat transfer, and mass transfer, and the finite-difference is most often used in mathematically based derivations.

In the discretized formulation, attention is focused on nodes and elements. The nodes are the selected points at which the numerical solution is to be obtained while the elements are volumes that fill the solution space. Nodes are distributed on the boundaries of the elements.

In an attempt to produce numerical simulations which more closely represent the actual physical processes, significantly higher nodal densities are employed to account for the many complex phenomena that often occur simultaneously. The resultant nodal densities are required in order to accurately resolve the complex variabilities in fluid flow pattern such as boundary layer flow, recirculation zones, steep pressure gradients, continuously but abruptly varying flow cross-sectional area, flow direction reversals, etc. In addition to these fluid flow intricacies, the current physical processes of interest contain heat transfer, mass flow, phase change, particle-capture modalities, and mechanical-device-driven flows. It is imperative to consider each of these phenomena when designing the mesh for the simulation as each of these processes may be more or less complex in specific zones. One zone may have a relatively simple fluid flow pattern, but the heat transfer or phase change in that zone may require elevated nodal densities to get the best solution from the simulation.

The overarching theme of this thesis research is biomedical therapeutic processes delivered by fluid-mechanic means. The specific applications all relate to fluid flow, but are otherwise unique within themselves. In one therapeutic application, the focus is directed to the migration of a drug substance from its zone of application to downstream locations under the dual action of advection and diffusion. In a second situation, a delivered medium undergoes a

phase change which produces thermal energy whose action is to elevate tissue temperatures and cause necrosis. The last of the applications is concerned with trajectories of medications in the form of particulates that are transported to their target locations through the respiratory system. Each of these applications requires unique modeling. The models involved present a kaleidoscope of different physical processes and phenomena.

The specifics of these applications will be dealt with serially. The relevant literature for each of the specific applications will be cited in the introduction section of the respective chapters in which the application is described.

The first application relates to drug-eluting stents. In general, a stent is a structure whose function is to maintain an artery as an open cross section for the flow of blood. This function is a necessary follow-on of a procedure called angioplasty. That procedure is employed when arteries become blocked by the deposition of plaque; plaque-blocked arteries are frequently termed stenosed. To return the artery to its proper function, the first step is to open the blockage. Although logic suggests that the opening of the blockage should be, somehow, related to the removal of the plaque, that is an uncommon event. In reality, a balloon, whose initial state is flaccid, is maneuvered through the cardiovascular system by means of a guide wire or a catheter and then brought to rest in a stenosed artery. Subsequently, the balloon is inflated, thereby pushing back the stenosed walls and opening the artery cross section. Experience has taught that that opening will not maintain itself. Consequently, a place holder made of a structurally strong medium is delivered to the site, again by means of a guide wire or catheter. A common configuration for the placeholder is a wireframe, termed a stent.

Since the stent is an intrusion into a biologically sensitive environment, it has been found that acceptance of the stent by the body is enhanced by coating the stent wireframe by a drug, for example, paclitaxel. The drug is encased in a polymer envelope. Upon placement of the stent, the drug diffuses through the

polymer and is dispersed, partially into the plaque and therefrom into the artery wall. In addition, some of the drug mingles with the flowing blood and is advected downstream. Owing to cross-stream diffusion, some of the advected drug is delivered to the downstream artery walls, and diffuses into them. The penetration of the drug into the artery wall at downstream locations is the focus of Chapter Two of this document.

The second application, addressed in Chapter Three, entails the study of an alternative therapeutic approach to treating menorrhagia which utilizes heat liberated from steam condensing on the uterine walls. There are many reasons for finding new, non-surgical, therapies for treating this condition that minimize the need for removing the uterus, a procedure known as a hysterectomy. There are several treatment options that involve the use of heat to achieve necrosis of the tissue [2]. If the heat source can be well controlled, both in temperature and spatial uniformity, it gives the patient a viable alternative to surgery. The process studied in this work utilizes steam as the heat source. As steam enters the cavity and comes into contact with the uterine walls, which are at a relatively colder temperature. The steam condenses and liberates a large quantity of latent heat. This heat then transfers into the tissue and begins to accumulate damage. The elevated temperatures are considered along with the duration of time to calculate the Henriques-Moritz damage integral, a widely accepted method of evaluating tissue damage. It is important to consider that tissue damage continues after the active application of steam, and this has significant impact on the depths of necrosis which result from the treatment.

The third treatment of interest involves delivering a drug that enters the respiratory system by inhalation through the nose or mouth and provides the motivation for Chapter Four. These drugs are often administered in extremely small liquid or solid particles, on the order of 10^{-6} m in diameter, from a nebulizer and are used to treat many different conditions. An important element in maximizing the efficacy of the drug is being able to predict where it will be

deposited once it enters the human respiratory system. If significant amounts of drug mass do not make it to the intended target, the treatment will have a greatly diminished effect. The drug particles are carried through the respiratory system by the air flow patterns that occur in the passageways. The flow path from the nose or mouth, through the throat and into the lungs is one of great complexity, encompassing many twists, turns, and changes in diameter along the way. The travel path of particles of this size is heavily influenced not only by the size and density of the particles, but also the fluid velocity and the geometry of the flow path.

To the best knowledge of the author, based on an exhaustive literature search, a methodology has yet to be developed to predict the trajectory of very small particles carried through an extremely complex flow path by a discrete rush of air. It is well understood that the geometry of the respiratory system is not only complex, but also differs among individuals based on age, gender, and physical condition, among other factors. In this light, the task undertaken here is not specific to any of these categories. Rather, the development is carried out for a geometry of sufficient complexity to ensure the applicability of the developed methodology to a variety of complex geometries.

Therefore, the focus of the work is the methodology development. To provide a quantitative means of identifying where particles of different sizes are collected at different locations, a model of a series of particle-collection impaction modules has been utilized. The efficacy of the modeled system will be quantified with respect to the precision with which particles of different sizes are collected on impaction plates.

CHAPTER 2 – MASS TRANSFER BY ADVECTION AND DIFFUSION FROM A DRUG-ELUTING STENT

INTRODUCTION

The use of cardiovascular stents has become an accepted medical procedure for maintaining the lumen in an open state after the angioplasty procedure has been used to unblock a stenosed artery. Early experience with the use of cardiovascular stents provided information about the body's acceptance of the stent. Furthermore, it was found that the presence of a stent could be a source of tissue damage in many cases. To deal with these issues, the use of drug-coated stents has been found to be effective. In practice, the drug is cocooned within a polymer. Mass transfer driven by concentration differences causes the drug to diffuse through the polymer. Subsequent to this diffusion process, the drug may be carried away by the blood passing through the lumen or may diffuse through the tissue layers that form the artery wall.

The distribution of the drug subsequent to its passage through the polymer has recently evoked considerable interest in the biomedical community. The first paper dealing with the distribution of the drug among the tissue layers of the artery wall and the transport of the drug by blood flow in the lumen was published in 2007 [3]. Subsequent publications appeared in 2009 [4] and 2010 [5]. These papers can be characterized as having a common approach. Each of them dealt with a specific case without recognition of the cases treated in the other papers. Earlier publications were focused on either the transport of the drug through the artery wall or into the blood flowing through the lumen but did not consider simultaneous transport.

Among the previous work that dealt with transport of the drug through the artery wall, a variety of models were employed. Three of these references formulated the problem in dimensionless form, but were based on primitive models. In [6], a model taking account of diffusion and of spatially independent velocity was

adopted without description of the process by which the velocity was created. In contrast, [7] is confined to a pure mass diffusion model. The approach of [8] is to treat the mass diffusion problem as an analogous heat conduction problem.

Other papers that are focused on drug diffusion through the artery wall dealt with specific values of the relevant parameters. A common denominator among the wall-focused transport approach was the use of a porous medium model [9-11]. In [12-13], the effect of compression of the artery wall was considered, while in [14, 15], the model included both diffusion through the polymeric coating and the arterial tissue. The case of drug transport by means of lumen blood flow is treated in [16] by a boundary layer model.

In the present work, the problem of drug transport both into the arterial wall and by the blood stream passing through the lumen is considered. The special feature of the present approach is to recast all of the governing equations and boundary conditions in dimensionless form and to investigate a broad range of the governing dimensionless parameters. This approach is a broad generalization of the limited previous work [3-5] to cover all of the possible cases that may occur in practice. The previous work may be regarded as special cases of the work performed here.

PHYSICAL MODEL

The description of the physical model is facilitated by reference to Figure 2.1. The figure shows a sideview of an axisymmetric artery in which a drug-eluting stent has been put in place. Although the stent is a ring which spans the entire circumference, in this view the stent appears as the darkened segments on the inner wall of the lumen. Dashed lines have been used to represent the ring-like geometry of the stent. The thickness of the stent is regarded as being very small compared with the thickness of the artery wall. The surface of the stent is coated with the eluting drug. The artery wall has a finite thickness.

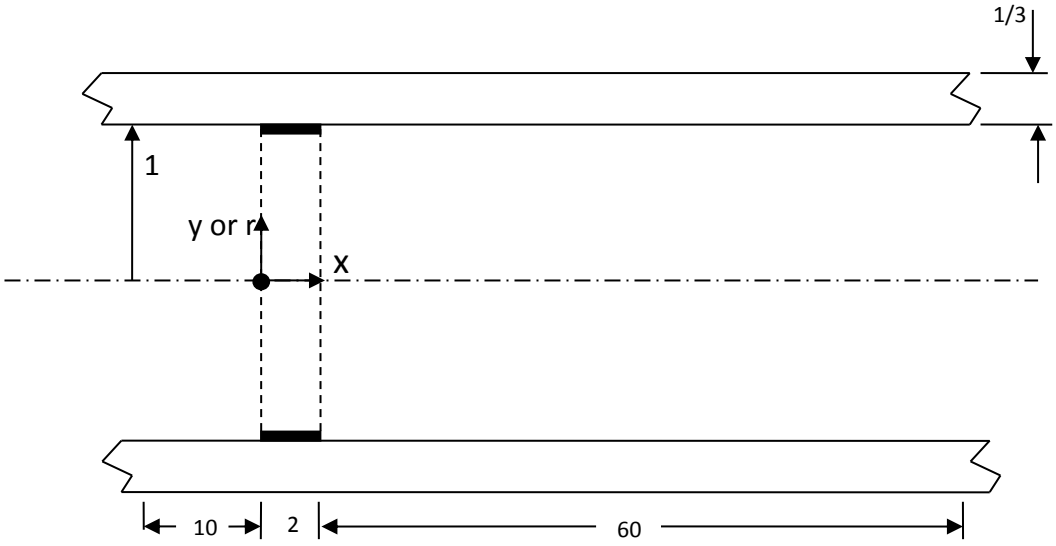

Figure 2.1 - Schematic side-view diagram of the physical system to be investigated.

The dimensions and coordinates that are called out in the figure are all non-dimensional. The *radius* of the lumen is the representative length chosen for the non-dimensionalization. Consequently, the dimensionless radius is one. As can be seen from the figure, the solution domain starts at a distance of 10 radii upstream of the stent and extends to a distance of 60 radii downstream. The stent itself has a streamwise length of two radii, and the thickness of the artery wall is one-third of the radius [4].

MATHEMATICAL MODEL

GOVERNING EQUATIONS

The mathematical model is conveniently described by using dimensionless variables. In the definition of these variables, reference quantities are needed for the velocities, coordinates, lengths, and pressure. These reference quantities are respectably, the mean velocity U', the internal radius of the lumen R', and the velocity head ($\rho' U'^2$). The physical variables will be distinguished by primes so that the dimensionless variables will be unprimed. The definitions of the dimensionless variables are

$x' = xR', y' = yR', z' = zR', r' = rR'$ (2.1)

$u' = uU', v' = vU', w' = wU'$ (2.2)

$p' = p(\rho' U'^2)$ (2.3)

$Re = (\rho' U' R')/\mu'$ (2.4)

Note that the Reynolds number Re is based on the internal radius of the lumen.

With these definitions, the dimensionless governing equations for laminar flow are

$$u\frac{\partial u}{\partial x} + v\frac{\partial u}{\partial y} + w\frac{\partial u}{\partial z} = -\frac{\partial p}{\partial x} + \frac{1}{Re}\left[\frac{\partial^2 u}{\partial x^2} + \frac{\partial^2 u}{\partial y^2} + \frac{\partial^2 u}{\partial z^2}\right] \quad (2.5)$$

$$u\frac{\partial v}{\partial x} + v\frac{\partial v}{\partial y} + w\frac{\partial v}{\partial z} = -\frac{\partial p}{\partial y} + \frac{1}{Re}\left[\frac{\partial^2 v}{\partial x^2} + \frac{\partial^2 v}{\partial y^2} + \frac{\partial^2 v}{\partial z^2}\right] \quad (2.6)$$

$$u\frac{\partial w}{\partial x}+v\frac{\partial w}{\partial y}+w\frac{\partial w}{\partial z}=-\frac{\partial p}{\partial z}+\frac{1}{Re}\left[\frac{\partial^2 w}{\partial x^2}+\frac{\partial^2 w}{\partial y^2}+\frac{\partial^2 w}{\partial z^2}\right] \quad (2.7)$$

Note that in these equations, the density ρ and the viscosity μ do not appear. Instead, in the position normally occupied by ρ in these equations, the coefficient 1 appears. By the same token, the position of μ as a multiplier of the viscous terms is now occupied by 1/Re. Therefore, for all fluids that are to be considered, it will be appropriate to set the density equal to one and the viscosity equal to 1/Re. This formulation enables the attainment of universal solutions.

There are two equations needed to represent the conservation of mass in the flowing fluid. One of these two equations is for conserving blood, the carrier fluid, and the other equation is for conserving the drug. Alternatively, mass may be conserved for the mixture as a whole, and a separate conservation equation may be written for the drug. The second of these alternatives is the one that is more commonly used in analysis. For the mixture as a whole, dimensionless mass conservation for an incompressible fluid can be expressed as

$$\frac{\partial u}{\partial x}+\frac{\partial v}{\partial y}+\frac{\partial w}{\partial z}=0 \quad (2.8)$$

For the conservation of the drug as a species, note must be taken of the two processes by which the drug is transported. One of these is the advective transport of a species by the bulk motion of the fluid, and the other is the transport by molecular diffusion. The corresponding dimensionless species conservation equation is

$$u\frac{\partial c}{\partial x}+v\frac{\partial c}{\partial y}+w\frac{\partial c}{\partial z}=\frac{1}{Pe}\left[\frac{\partial^2 c}{\partial x^2}+\frac{\partial^2 c}{\partial y^2}+\frac{\partial^2 c}{\partial z^2}\right] \quad (2.9)$$

In this equation, the quantity c is the dimensionless concentration of the drug and Pe is the Peclet number, which are respectively defined as

$$c = \frac{c'}{c_0{}'},\ Pe = ReSc,\ Sc = \frac{\nu'}{D'_{fluid}} \tag{2.10}$$

where c_0' is the given concentration of the drug at the surface of the stent; Sc, v', and D'_{fluid} are respectively the Schmidt number, kinematic viscosity, and the binary diffusion coefficient, all for the fluid mixture.

The present model does not take account of convective motion in the artery wall, so that diffusion is the sole means of mass transfer. Therefore, the governing equation for mass transfer in the wall reduces to

$$\left[\frac{\partial^2 c}{\partial x^2} + \frac{\partial^2 c}{\partial y^2} + \frac{\partial^2 c}{\partial z^2}\right] = 0 \tag{2.11}$$

BOUNDARY CONDITIONS

In the model adopted here, the stent is envisioned as a very thin ring whose infacing (lumen-facing) surface is at the concentration c_0'. The outfacing surface of the stent is in perfect contact with the artery wall. The stent has a radius R, equal to that of the lumen, and has a streamwise length that is 2R. With regard to the artery wall, it extends upstream and downstream from the stent by 10 and 60 radii, respectively. These dimensions define the solution domain in which the problem is solved. At the inlet of the solution domain (x = -10), the velocity distribution in the lumen is parabolic and steady, and the concentration of the drug is zero both in the lumen and in the artery tissue.

The downstream end of the fluid portion of the solution domain is defined by very weak boundary conditions which are, specifically, that the streamwise second derivatives are zero for all the velocity components and the concentration. Experience has taught that the specification of these weak boundary conditions provides ample freedom for the fluid flow and mass transfer to be very lightly constrained. The other fluid-flow boundary condition at the downstream end of the solution domain is a prescribed pressure, which is here taken to be zero (gauge pressure). The downstream end of the artery wall is defined by a no-mass-flow boundary condition. In addition, the artery wall imposes a no-slip condition on the tangential component of the velocity and an impermeability condition for the normal component of the velocity.

The mass transfer boundary conditions at the upstream and downstream ends of the solution domain have already been discussed, as has the assigned uniform concentration at the lumen-facing surface of the stent. It remains to deal with the concentration boundary conditions at the interface between the lumen and the tissue which comprises the artery wall. Also needed is a boundary condition at the rear face of the artery wall. At the lumen-tissue interface, continuity of mass flux is required, so that in terms of physical variables

$$\left(\mathrm{D}'\frac{\partial c'}{\partial r'}\right)_{fluid} = \left(\mathrm{D}'\frac{\partial c'}{\partial r'}\right)_{tissue} \tag{2.12}$$

A second condition at the interface representing a discrete interfacial resistance was taken from [4]. It is

$$\left(\mathrm{D}'\frac{\partial c'}{\partial r'}\right)_{fluid} = \left(\mathrm{D}'\frac{\partial c'}{\partial r'}\right)_{tissue} = h_m'\,(c'_{tissue} - c'_{fluid}) \tag{2.13}$$

In these equations, D' is the mass diffusion coefficient, and ($1/h_m'$) is the discrete resistance. The quantities c'_{tissue} and c'_{fluid} correspond, respectively, to the concentrations of the drug on either side of the discrete resistance. There is a jump of concentration equal to the difference between these concentrations. At any arbitrary streamwise location, both c'_{tissue} and c'_{fluid} are unknown. However, at the stent, $c'_{fluid} = c_0'$.

To facilitate a numerical solution of the governing equations, it is appropriate to rephrase the physical boundary conditions in mathematical and dimensionless terms.

(a) At the upstream end of the solution domain

$$u = 2(1 - r^2),\ c = 0 \tag{2.14}$$

for the lumen, and $c = 0$ in the artery wall.

(b) At the surface of the lumen at all streamwise locations

$$u = 0,\ v = 0,\ w = 0 \tag{2.15a}$$

and for the concentration at the lumen-tissue interface

$$\left(\frac{\partial c}{\partial r}\right)_{fluid} = \frac{\mathrm{D}_{tissue}}{\mathrm{D}_{fluid}}\left(\frac{\partial c}{\partial r}\right)_{tissue} \tag{2.15b}$$

with the additional discrete resistance

$$\left(\frac{\partial c}{\partial r}\right)_{fluid} = \Gamma\left(c_{tissue} - c_{fluid}\right) \tag{2.15c}$$

$$\Gamma = \frac{h_m{}' R}{\mathrm{D}'_{fluid}} \tag{2.15d}$$

The quantity Γ is a dimensionless group which resembles the Biot number for heat transfer.

(c) At the lumen wall and at the location of the stent, *0 ≤ x ≤ 2*,

$$c = 1 \tag{2.16a}$$

and

$$\left(\frac{\partial c}{\partial r}\right)_{fluid} = \Gamma(c_{tissue} - 1) \tag{2.16b}$$

(d) The downstream closure for the fluid at *x = 62* is

$$\frac{\partial^2 u}{\partial x^2} = \frac{\partial^2 v}{\partial x^2} = \frac{\partial^2 w}{\partial x^2} = \frac{\partial^2 c}{\partial x^2} = p = 0 \tag{2.17a}$$

and in the artery wall

$$\frac{\partial c}{\partial x} = 0 \tag{2.17b}$$

(e) At the back face of the artery wall

$$\frac{\partial c}{\partial r} = 0 \tag{2.18}$$

NUMERICAL SIMULATION

The governing differential equations and boundary conditions were discretized and solved numerically by CFX software. The discretization is performed by the finite-volume approach. Although the problem, as formulated here, is axisymmetric, CFX does not have an axisymmetric option. Therefore, it is necessary to create a three-dimensional version of the two-dimensional axisymmetric situation. This geometric extension is achieved by creating a wedge of very small opening angle whose radial sides are symmetry planes and whose rim is an arc of the artery wall. A schematic diagram of the wedge geometry is displayed in Figure 2.2. The wedge angle that was selected for the solution is 2°.

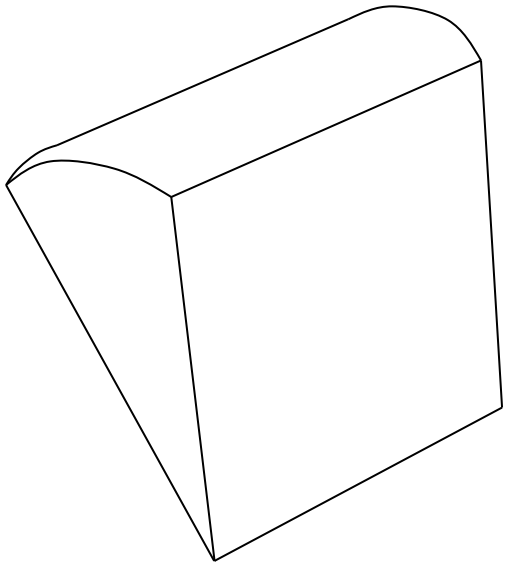

Figure 2.2 - Wedge of small opening angle representing a symmetry module.

The flow was regarded as laminar. The discretization of the solution domain gave rise to a mesh encompassing 344,613 nodes and 170,500 elements. Mesh independence calculations were performed by redeployment of the nodes so as to create a much more dense mesh in the near neighborhood of the wall. The

two investigated meshes gave rise to wall mass transfer results that agreed to within 0.2%. The surface mesh of the solution domain is exhibited in Figures 2.3 and 2.4. It can be seen from the figure that a graduated mesh was used adjacent to the lumen-tissue interface with particular concentration of elements in the neighborhood of the stent

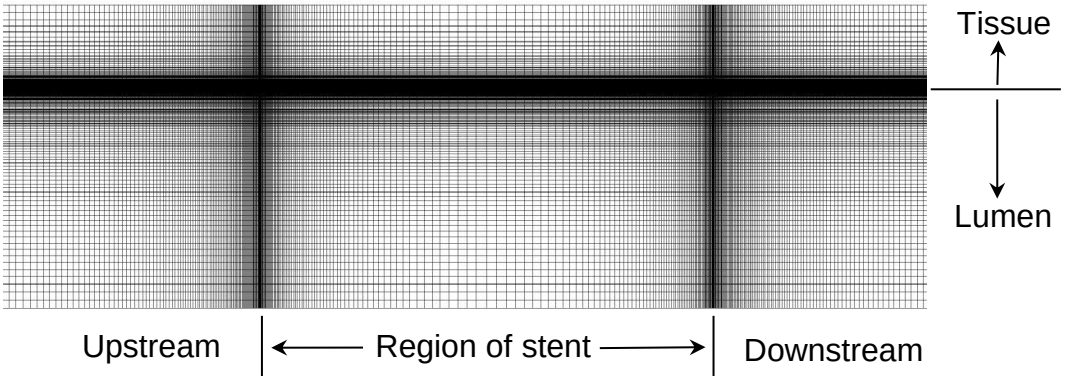

Figure 2.3 – Mesh used for the numerical solutions. The darker areas illustrate the areas of significantly higher mesh densities.

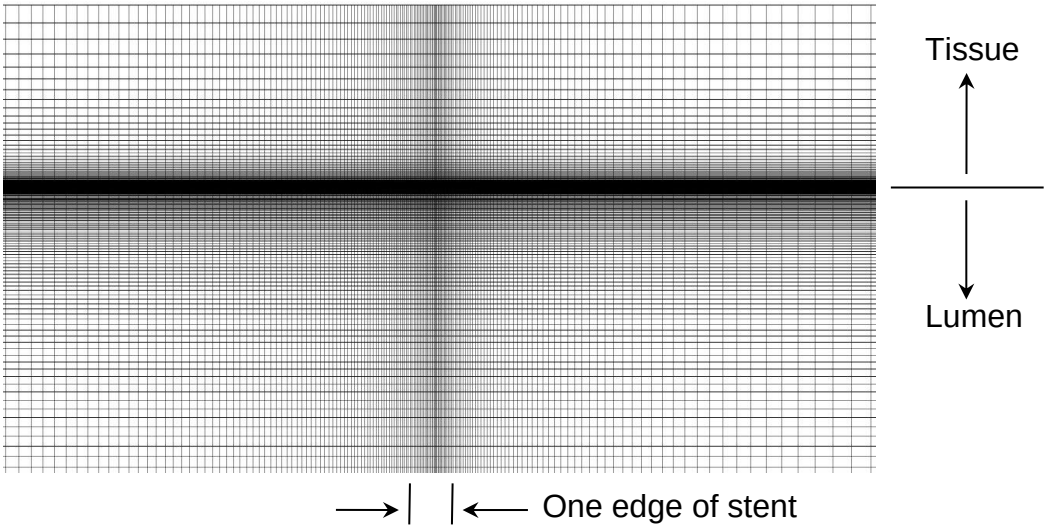

Figure 2.4 - Mesh used for the numerical solutions. The dark horizontal line is due to the dense concentration of elements in the neighborhood of the lumen-tissue interface.

RESULTS AND DISCUSSION

The first set of results to be presented is the rate of mass transfer from the medicated stent to the flowing fluid. The local mass flux $\dot{m}$ at the infacing surface of the stent is given by Fick's Law, which is

$$\dot{m} = -\mathrm{D}'_{fluid}\frac{\partial c'}{\partial r'} \tag{2.19}$$

The derivative is taken at r' = R. With the introduction of the dimensionless variables and coordinates, Eq. (2.19) becomes

$$\left(\frac{\dot{m}}{c'_o}\right)\left(\frac{R}{\nu}\right) = [f(x)]Re,\ 0 \le x \le 2 \tag{2.20}$$

where Re is the Reynolds number. In this equation, f(x) represents a dimensionless derivative taken from the numerical solutions. Its value depends on Re, Sc, and the other parameters that appear in Eq. (2.15). If $(\dot{m}/c'_o)$ is regarded as a local mass transfer coefficient, then the left-hand side of Eq. (2.20) is similar to a local Sherwood number with the kinematic viscosity replacing the mass diffusion coefficient.

The average mass flux $\overline{\dot{m}}$ passing from the surface of the stent to the lumen fluid can be obtained by integration of Eq. (2.20), with the result

$$\left(\frac{\overline{\dot{m}}}{c'_o}\right)\left(\frac{R}{\nu}\right) = gRe \tag{2.21}$$

where *g* depends on the Reynolds number Re and the Schmidt number Sc.

Attention will next be turned to the numerical results and parametric dependencies of the average mass flux passing from the stent to the lumen fluid as given by Eq. (2.21). The role of the Biot-number-like parameter Γ of Eq. (2.15d) was first investigated. Values of Γ between 0.000008 and 100 were assigned for Re between 25 and 500 and for Sc between 2000 and 200000. It was found that $\overline{\dot{m}}$ was completely insensitive to Γ. Next, the ratio of the diffusion

coefficients that appear on the right-hand side of Eq. (2.15b) was assigned a fixed value of 0.0511 [4].

The final solutions yielding $\overline{\dot{m}}$ were performed for Re values between 25 and 500 and for Sc between 2000 and 200,000. Power-law fits of high accuracy provided the compact representation

$$\left(\frac{\overline{\dot{m}}}{c'_o}\right)\left(\frac{R}{\nu}\right) = 0.0707 Re^{0.33} Sc^{-2/3} \tag{2.22}$$

or

$$\left(\frac{\overline{\dot{m}}}{c'_o}\right)\left(\frac{R}{\mathrm{D}_{fluid}}\right) = 0.0707 (ReSc)^{1/3} \tag{2.23}$$

The compactness, simplicity, and generality of this result are witnesses for its usefulness.

The results for the local mass transfer rates passing from the inward-facing surface of the medicated stent to the lumen are presented in Figs. 2.5(a-d). In each figure, the dimensionless local mass transfer rate which appears on the left-hand side of Eq. (2.20) is plotted as a function of the dimensionless axial coordinate x in the range $0 \leq x \leq 2$. Each figure encompasses a main portion and an inset. The main portion provides results for x between -0.02 and 0.1, while the inset spans the entire range between 0 and 2. The reason for this dual presentation is to provide detailed results at the forward edge of the stent as well as results for the stent's entire streamwise length. Each figure corresponds to a discrete Reynolds number between 25 and 500.

An overview of Figs. 2.5 reveals certain trends that are consistent among all of the figures. The most apparent of these is that the highest rates of mass transfer occur in the neighborhood of the upstream edge of the stent. In all cases, there is evidence of diffusive mass transfer carrying the drug upstream of the leading edge of the stent. The high mass transfer peak decreases very sharply and for

most of the length of the stent, the mass transfer rates are a small fraction of the maximum. Another very strong trend is the increase of the rate of mass transfer with increasing values of the Reynolds number. This trend is readily identified by observing the mass transfer maxima at each of the Reynolds numbers. These maxima are approximately 0.3, 0.45, 0.55 and 0.68, respectively for Re = 25, 112, 250 and 500. The effect of Reynolds number pervades the results over the entire longitudinal extent of the stent.

Also strongly in evidence is the effect of the Schmidt number. The rate of mass transfer diminishes sharply with increasing Schmidt number. This characteristic can be attributed to the fact that mass transfer increases as the diffusion coefficient increases. Since the diffusion coefficient appears in the denominator of the Schmidt number, the trend is entirely plausible. Quantitative evidence of the Schmidt number effect can be obtained by comparing the peak values of the mass transfer rate at various Schmidt numbers. For example, for Re = 25, the successive peaks in the mass transfer rate are approximately 0.3, 0.05 and 0.01 as the Schmidt number is varied from 2000 to 20,000 to 200,000. For Re = 500, a similar comparison yields peak mass transfer rates of about 0.66, 0.1 and 0.013.

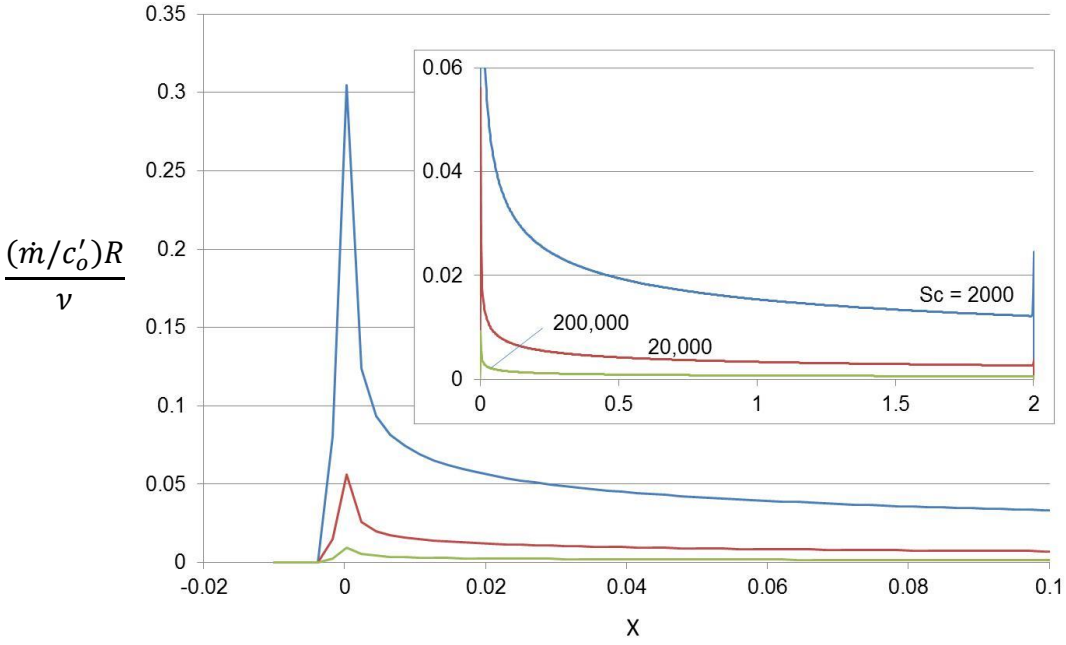

Figure 2.5(a) - Local mass transfer rates from the inward facing surface of the stent to the lumen, Re = 25.

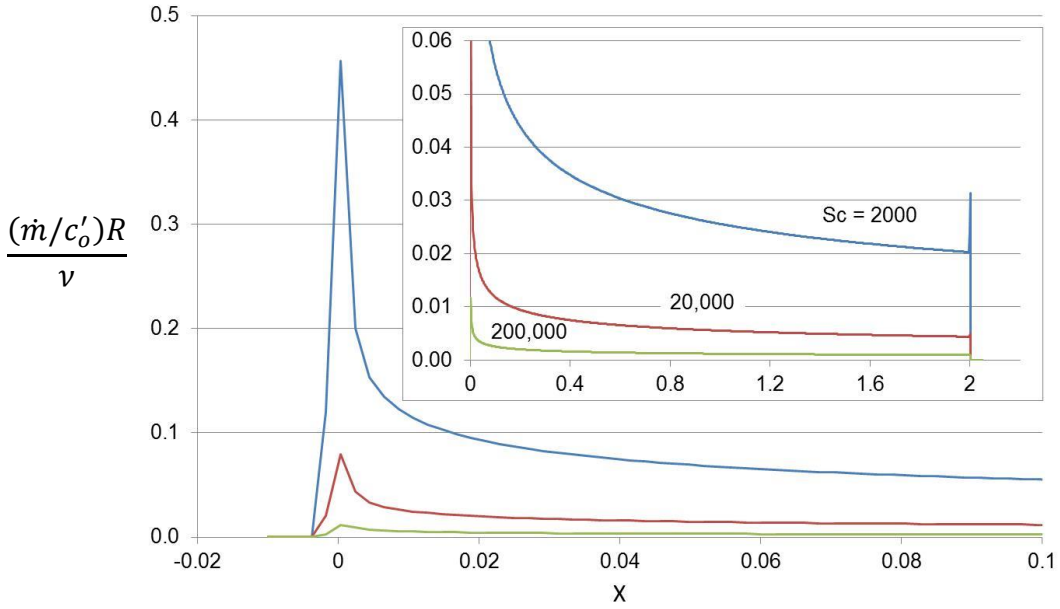

Figure 2.5(b) - Local mass transfer rates from the inward facing surface of the stent to the lumen, Re = 112.

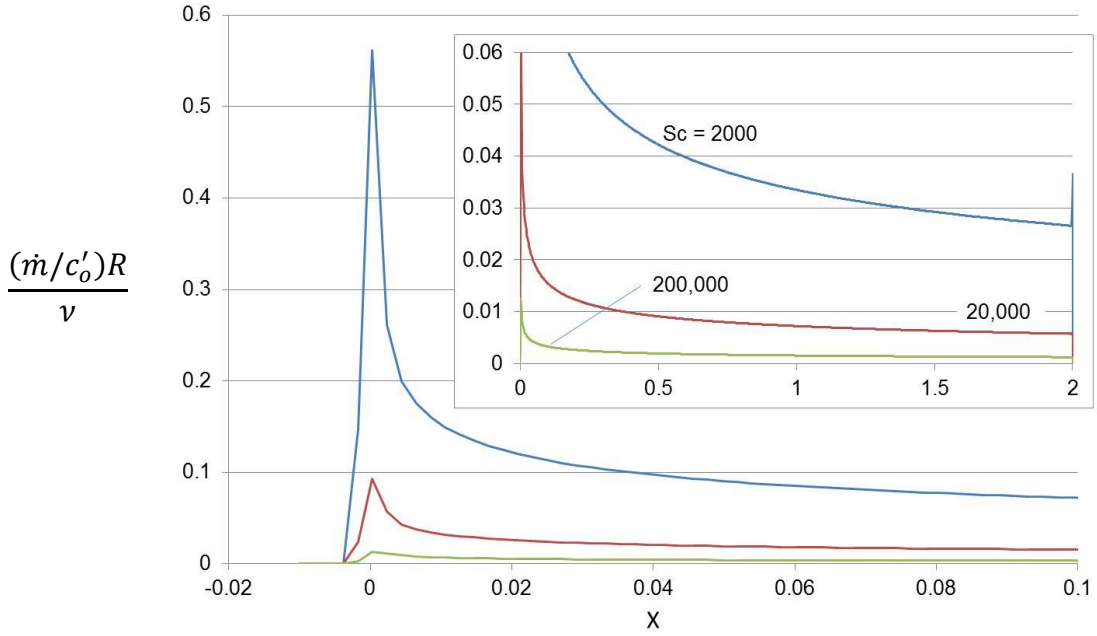

Figure 2.5(c) - Local mass transfer rates from the inward facing surface of the stent to the lumen, Re = 250.

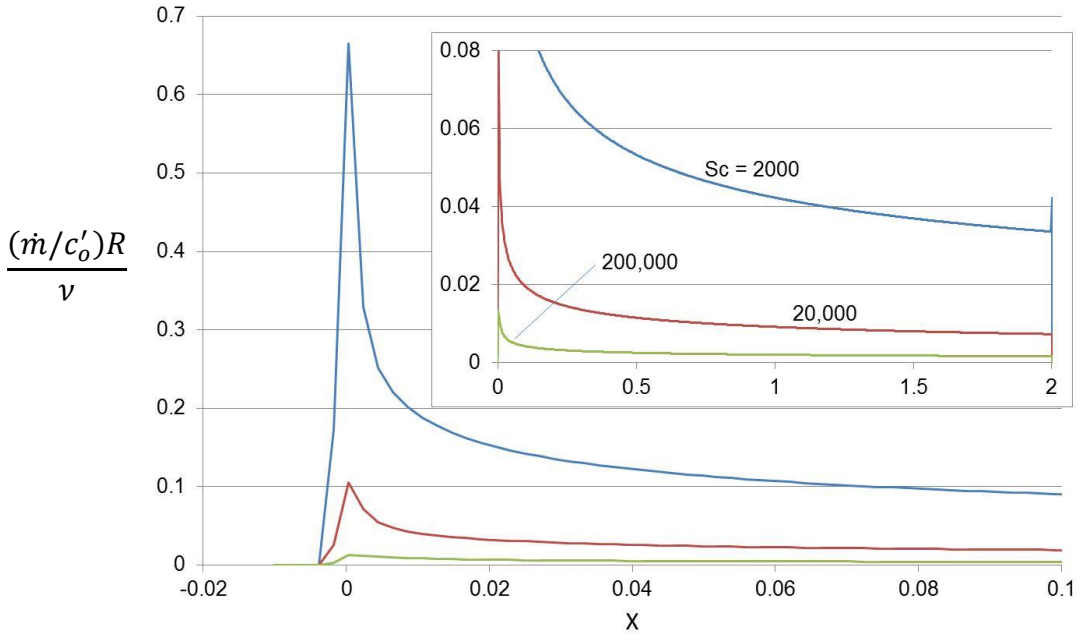

Figure 2.5(d) – Local mass transfer rates from the inward facing surface of the stent to the lumen, Re = 500.

The local mass flux from the outward-facing surface of the stent to the tissue is exhibited in Figs. 2.6(a) and 2.6(b). Two figures are sufficient to convey these results since they are virtually independent of the Reynolds number. Figures 2.6(a) and 2.6(b) respectively correspond to Reynolds numbers of 112 and 500. A careful examination of the ordinate values of these figures indicates that the difference in the mass transfer rates at the two Reynolds numbers is of no practical significance.

It is useful to compare the mass transfer rates to the lumen and to the tissue. From a comparison of Figs. 2.5 and 2.6, it is seen that the mass transfer to the lumen flow considerably exceeds that to the tissue. It may, therefore, be concluded that a major part of the drug is not fulfilling its intended purpose. Another point of difference between Figs. 2.5 and 2.6 is the behavior upstream of the leading edge of the stent. Figures 2.6 show that the drug is actually flowing from the wall into the lumen in the upstream region. This process can be explained by noting that diffusion occurs in all directions, so that drug that enters the wall that is contact with the stent is able to diffuse within the wall to locations where $x < 0$. At those locations, the concentration of drug within the wall is greater than that in the lumen, thereby giving rise to an outflow of the drug from the wall to the lumen. The magnitude of this outflow is too small to be seen within the scale of the ordinate of Fig. 2.5.

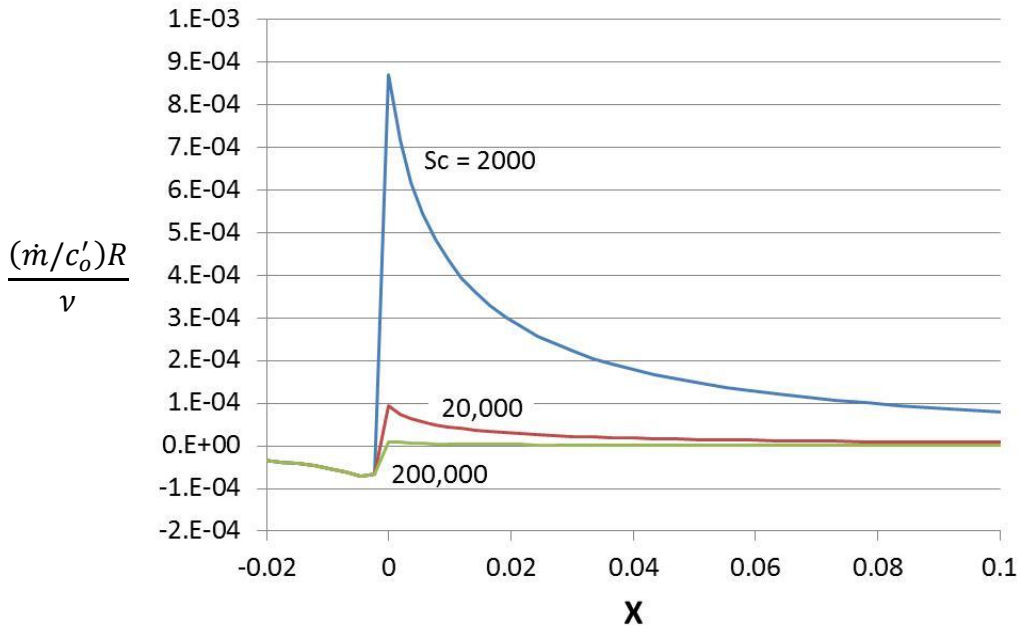

Figure 2.6(a) – Local mass transfer rates from the outward facing surface of the stent to the tissue, Re = 112.

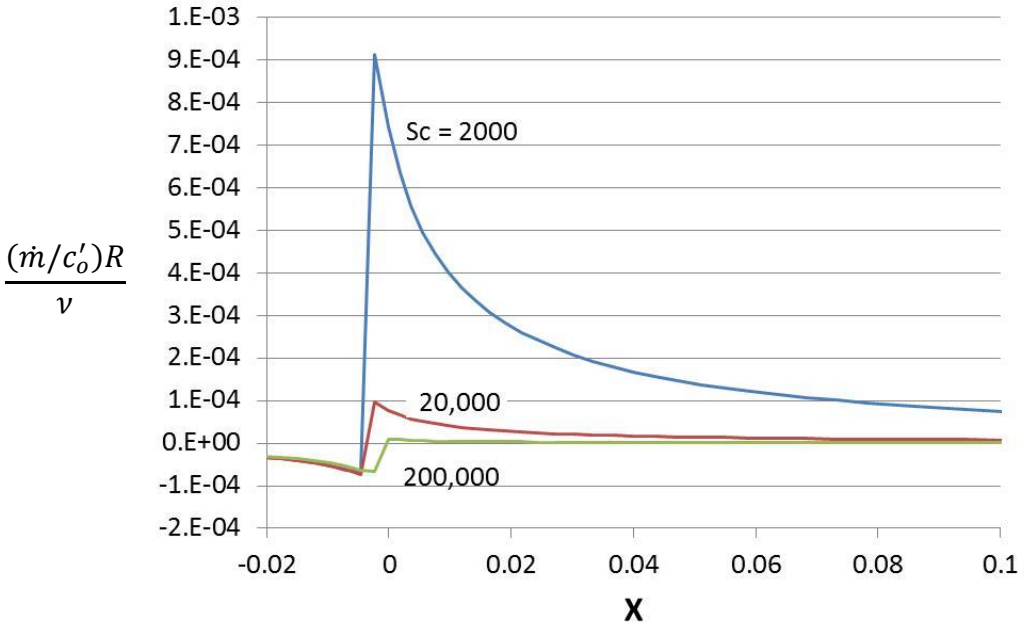

Figure 2.6(b) – Local mass transfer rates from the outward facing surface of the stent to the tissue, Re = 500.

CONCLUDING REMARKS

The transport of a drug from the surfaces of a medicated stent to blood flowing in the adjacent lumen and to the artery wall that contacts the stent has been determined by means of numerical simulation. The physical processes encompassed by the model are fluid flow and advective/diffusive mass transfer in the lumen, diffusive mass transfer in the artery wall, and interfacial mass transfer resistance at the lumen-wall interface. Previous work in the field had been restricted to special cases characterized by specific numerical values of the relevant parameters. The present formulation is based on dimensionless variables and parameters with Reynolds number, Schmidt number, and a mass-transfer Biot number as parametric groupings. The dependent dimensionless grouping is a Sherwood number.

A wide range of numerical values, spanning all realistic conditions, was assigned to the parametric groupings. It was found that the Sherwood number results were not affected by the mass-transfer Biot number, thereby eliminating the interfacial resistance from further consideration. If the Sherwood number were to encompass the mass diffusion coefficient, as is conventional, then the average Sherwood number for the mass flux from the stent to the lumen flow was found to depend on the product of the Reynolds and Schmidt numbers to the one-third power.

The local mass transfer rates from the stent to both the lumen flow and to the contiguous artery wall were greatest near the forward edge of the stent. The lumen-side results depended on the Reynolds number, while the wall-side results were virtually independent of the Reynolds number.

CHAPTER 3 – A UTERINE TISSUE ABLATION MODEL AND ITS IMPLEMENTATION

INTRODUCTION AND BACKGROUND

Menorrhagia, or Hematomunia, is a condition that results in abnormally heavy bleeding during regular menstrual cycles. This condition is typically used to describe bleeding that lasts longer than seven days, or produces greater than 80 mL of blood [17]. The condition affects more than ten million American women each year. In many cases, the direct cause for Menorrhagia is not known. Some of the potential causes include hormonal imbalance, uterine fibroids, dysfunction of the ovaries, or the development of polyps.

There is a wide variety of treatment options for Menorrhagia. The selection of the treatment will depend on many factors including the cause for the condition, the woman's age, general health condition, and medical history. Some women find relief from drug treatments such as ibuprofen, iron supplements or hormone therapy, but this approach is not curative. More curative approaches include surgical treatments such as dilation and curettage, operative hysteroscopy, endometrial ablation, or hysterectomy. The most permanent of these treatment options is hysterectomy. During this procedure, the uterus is partially or completely removed. The procedure results in the patient being unable to conceive a child, and also has surgical procedural risks. As a result of these effects, most women leave the hysterectomy as only the final option.

A schematic diagram showing the different extents of the hysterectomy procedure. The normal extraction of tissue material is defined by the orange long-dashed line shown in Figure 3.1. A more radical extraction is also illustrated in the figure as well as a more minimal tissue removal.

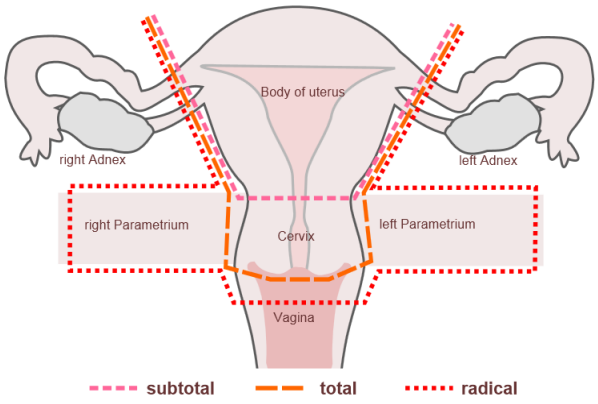

Figure 3.1 – Diagram depicting different extents of hysterectomy procedures

Ablation of endometrium that constitutes the inner lining of the uterine cavity has gained acceptance as a means for remediation of menorrhagia. An effective means for achieving this outcome is to impose elevated temperatures on the endometrial tissue for a duration of time that is sufficient to bring about cell necrosis. In addition to the means to achieve the necessary temperature level previously discussed, a new method of the injection of elevated-temperature fluids into the uterine cavity is considered in this work. A candidate fluid of considerable promise is steam (water vapor). Its unique feature is the high concentration of thermal energy that is characteristic of the vapor phase. The easy extraction of the concentrated thermal energy by means of condensation enables high rates of heat transfer to be applied to the walls of the uterine cavity. In this study, detailed numerical simulations are used to evaluate the duration of time required to achieve the desired depths of necrosis. Attention is also given to the uniformity of the depth of necrosis along the uterine lining.

There are several procedural options for removing the localized effected tissue, categorized as endometrial ablation. Cryotherapy is a treatment that uses low temperatures to achieve the desired necrosis. At the temperatures utilized in this procedure, on the order of -100°C, the tissue fluids freeze. Since these fluids are

water-based, they expand during the phase change from liquid to solid. This procedure is implemented by causing the tip of a small probe, which is inserted into the uterus, to attain the desired temperatures. The probe is guided to its target location by means of ultrasonic imagery. The probe tip is cooled by either flowing liquid nitrogen through it, or by expanding a compressed gas, causing the localized temperature reduction.

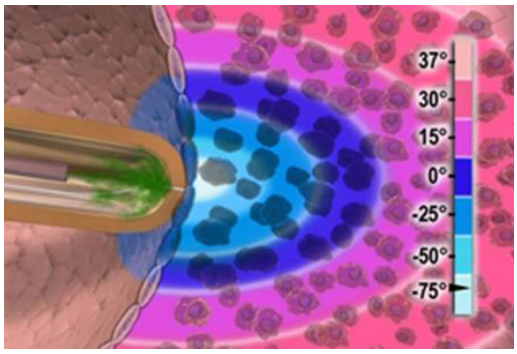

Figure 3.2 – Illustration of implementation of cryosurgical necrosis of dysfunctional tissue.

In its present utilization, cryosurgical implementation is based on the usage of gases such as argon, nitrous oxide and carbon dioxide [2]. These gases become cryo media due to the Joule-Thomson effect. This effect occurs when the gas flows adiabatically in a capillary tube of very small diameter. The concomitant pressure drop (of the order of a factor of seven) initializes the effect. An ideal gas is immune from the Joule-Thomson effect, but it is well known that there are certain ranges of pressures and temperatures within which almost all gases relinquish ideal gas behavior. The setup for the implementation of argon-based cryosurgery is shown schematically in Figure 3.3. As seen there, argon, contained in a high pressure container, flows through a capillary tube where it experiences a pressure drop large enough to activate the Joule-Thomson effect. The proximal end of the capillary tube is open, and the low temperature argon gas expands into an enlarged space. The rapid expansion induces shock waves

(not shown in the diagram). After the expansion, the flow turns sharply and enters an annular space which conveys it to exit ports.

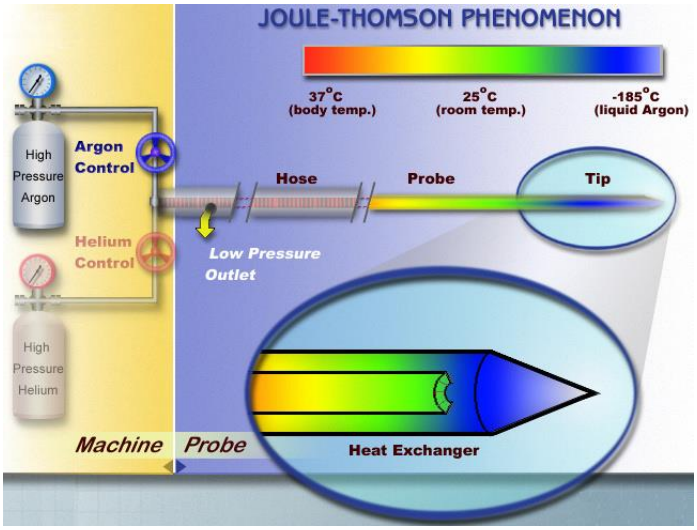

Figure 3.3 – Setup of the apparatus for the application of cryosurgery involving argon.

An alternative to the cryo-based ablation, there are a number of procedures based on the use of elevated temperatures. The temperature elevation may be achieved by electrocautery, hydrothermal pumping, balloon therapy, radiofrequency and microwave ablation, and the new methodology to be assessed in detail in this work. To implement electrocautery, an electric current passes through a wire loop or rollerball that is applied to the endometrial lining to cauterize the tissue [18]. The implementation of this therapy is illustrated in Figure 3.4 where the rollerball can be seen.

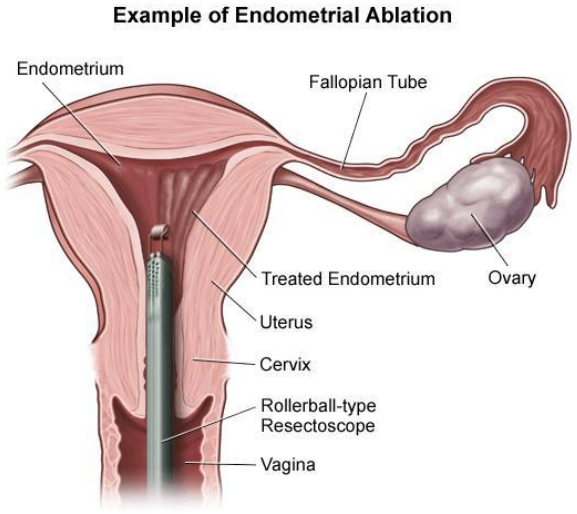

Figure 3.4 – Application of electrocautery by means of a rollerball.

The hydrothermal procedure is based on heated fluid being pumped into the uterine cavity to destroy the endometrial lining [2]. This procedure is illustrated in Figure 3.5.

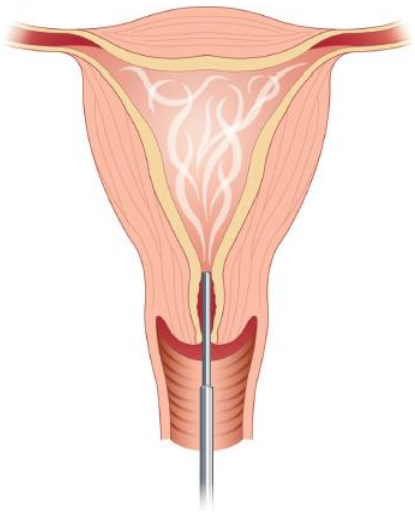

Figure 3.5 – Hydrothermal method of tissue ablation. [19]

For balloon therapy, a balloon at the end of a catheter is inserted into the uterus and filled with a fluid (liquid or gas) which has been heated to temperatures that cause tissue necrosis. The execution of this approach is shown schematically in Figure 3.6. The figure shows the balloon in intimate contact with the endometrial lining.

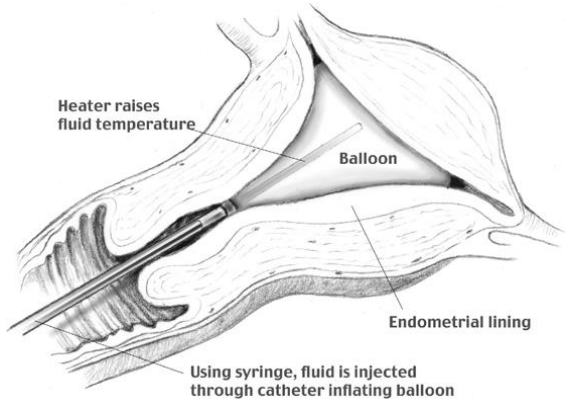

Figure 3.6 – Implementation of balloon therapy. [20]

To accomplish radiofrequency ablation, a triangular mesh electrode is expanded to fill the uterine cavity. The electrode delivers electrical current and destroys the endometrial lining [2, 21]. A diagram, Figure 3.7, illustrates the general approach which is widely used for thermally based alternatives to scalpel-based surgery. The electromagnetic energy is converted to thermal energy.

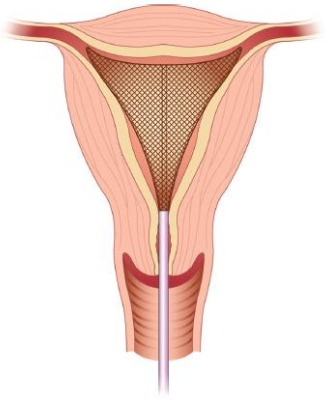

Figure 3.7 – General setup for radiofrequency ablation [19]

Microwave heating is based on the same principle as radiofrequency heating. The implementation of microwave ablation is the delivery of microwave energy through a slender probe that has been inserted into the uterus and destroys the endometrial lining [2, 22-24]. Figure 3.8 illustrates the mode of application of this heating methodology.

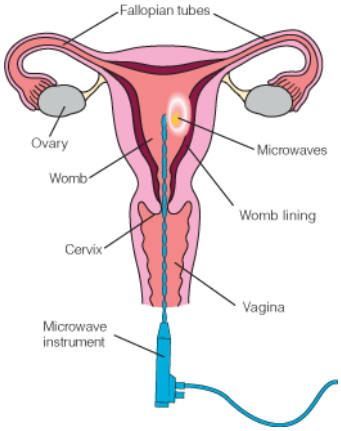

Figure 3.8 – Microwave heating modality.

METRICS FOR QUANTIFYING ELEVATED-TEMPERATURE TREATMENT MODALITIES

The goal of any of the aforementioned procedures is to cause enough damage to the subject tissue to kill the cells, or otherwise referred to as achieving necrosis. Collagen is in high abundance and is, therefore, assumed to be one of the main proteins that are involved with thermal damage at these higher temperatures. The typical thermal damage process is protein denaturation that follows a first-order chemical reaction. It is well-established that the conditions that bring about cell necrosis involve both the temperature level and the length of time over which the temperature is applied. The amount of time required to reach necrosis varies inversely to the temperature that is used. Higher treatment temperatures will achieve necrosis faster than lower treatment temperatures.

Generally, elevated-temperature thermal-based treatments are subdivided into two groups with respect to the targeted tissue temperature. Tissue temperatures above 50°C are reserved for direct treatment, and the therapy is termed *ablation*. When the target temperatures are between 40 and 45°C, the term *hyperthermia* is used to describe the therapy [25, 26].

Ablation therapy relies on the direct cytotoxic effect of temperature elevation. This mechanism of cell death is related to denaturing both functional and structural proteins (intra and extra cellular) [26]. The major extra-cellular structural protein constituent is collagen of various types, all with similar sensitivities to thermal injury [27, 28]. Thermal denaturation of collagen is a high-temperature metric of severe thermal damage and represents an upper-bound target process in ablation treatments that, when reached, is a sure sign of cellular death and severe vascular disruption.

Hyperthermia-based therapies rely on elevating the tissue temperature to relatively noncytotoxic levels to alter the local physiological environment and/or

cellular functions in a way that enhances other treatments. The details of these changes are extensive and have been reviewed elsewhere [25, 26, 29, 30]. The dominant physiological changes involve improved blood flow and oxygenation, stimulation of immune cell migration, and increased vascular permeability.

Independent of the heating method used, standardized metrics are needed to quantify dosage requirements to achieve desired outcomes. This is particularly important when comparing results from different studies, quantifying tissue-dependent sensitivities to heat, or attempting to repeat studies for the purpose therapeutic implementation. Two methods have come into general use for quantifying the deposited thermal energy. The ablation community often uses the damage index, whereas the hyperthermia community typically uses cumulative equivalent minutes at 43°C, or the *CEM°43* method [26, 30, 31]. Both the damage index and CEM°43 methods are based on the underlying premise that tissue damage follows an irreversible first-order chemical reaction with the rate constant following the Arrhenius relationship. Despite this commonality, the two methods are used differently: one to predict the degree of necrosis and the other to guide treatment duration.

CEM43°C METHOD

Cumulative equivalent minutes of thermal treatment at 43°C (CEM°43) (first proposed by Sapareto and Dewey [31]) is commonly used as a standard in the hyperthermia literature to compare different thermal treatment histories to an equivalent heating time at 43 degrees C. This procedure is discussed in depth in [26, 30]. Although the analysis is based on the assumption that thermal damage follows an irreversible first-order chemical reaction, experimental data have demonstrated that observed damage is approximately linear with temperature over a narrow range. Additionally, the dose response curve has inflection points

("breaks"); the break is related to increased tolerance to thermal injury that is developed during heating [26, 30]. There is insufficient data for human tissue to accurately define the breakpoint; most data show that it varies from 43.5 to 47°C [26, 30]. However, Lepock et al. [32] concluded that 43°C in cell culture likely represents the upper limit at which thermal tolerance can be induced in human cells.

Because of the presence of a breakpoint, the calculation of CEM°43 has to occur in two steps using Eq. (3.1) separately above and below the breakpoint.

$$\boldsymbol{CEM43°C = t[R_{CEM}]^{(43-T)}} \tag{3.1}$$

The symbol *t* is the time of thermal exposure. The time-scaling ratio R_{CEM} is the number of minutes needed to compensate for a 1°C change in the applied therapeutic temperature, either above or below the breakpoint, and *T* is temperature in degrees Celsius. The breakpoint of 43.5°C is chosen here, with an R_{CEM} below the breakpoint of 0.233 and above the breakpoint of 0.428.

Eq. (3.1) can also be used in a differential and/or a discretized form if the thermal history is dynamic and known.

$$\boldsymbol{CEM43°C = \int_0^{\tau}[R_{CEM}]^{(43-T(t))}dt = \sum_{i=1}^{N}[R_{CEM}]^{(43-T_i)}\Delta t_i} \tag{3.2}$$

However, the process of integration/summation has to account for temperatures that occur both above and below the breakpoint.

DAMAGE INDEX/INJURY INTEGRAL METHOD

The second metric used to quantify thermal exposure and cell injury is the

damage index Ω. This metric has been widely adopted by tissue ablation practitioners. Thermal ablation is generally accomplished at higher temperatures than is hyperthermia. Collagen is in high abundance and is, therefore, assumed to be one of the main proteins that are involved with thermal damage at these higher temperatures. The typical thermal damage process is protein denaturation that follows a first-order chemical reaction. The reaction state equation, combined with the temperature-dependent reaction rate, gives

$$\boldsymbol{Damage\ Integral} = \ \boldsymbol{\Omega(x,t) = ln\left(\frac{C(0)}{C(t)}\right) = A\int_0^t e^{-\left(\frac{\Delta E}{RT}\right)} d\lambda} \qquad (3.3)$$

C(0) – number of undamaged cells at the start of the treatment

C(t) – number of undamaged cells at the end of the treatment

A and ΔE – values determined experimentally and found in the literature

R – universal gas constant, which is 8.314 kJ/kmole-°K

t – time (seconds)

T – temperature in absolute units (°K)

It can be seen from the foregoing equation that the conditions that bring about cell necrosis involve both the temperature level and the length of time over which the temperature is applied, referred to as dose. The amount of time required to reach necrosis varies inversely to the temperature that is used. Higher treatment temperatures will achieve necrosis faster than lower treatment temperatures.

A numerical value of this integral of Ω = 0.53 is regarded as the onset of irreparable tissue damage and numerical values that are equal to or greater than one are widely accepted as characteristic of complete necrosis [33]. While each treatment instance has its own requirements, typical desired depths of necrosis

are 3-5 mm as it is reported that endometrium regeneration will not occur at depths greater than 2 mm [18].

Relationship Between the Two Methods

The CEM°43 and the Damage Index both originate from Arrhenius' experimental observations in the 1880s [34, 35]. The results and their interrelationship are very well described by [36, 37-39].

Eyring's introduction of the activation energy concept in the 1930s [37-41], that the reactants must surmount an activation energy barrier in order to form product, explained Arrhenius' experimental observations and resulted directly in the theory of absolute reaction rates.

When the time-scaling ratio R_{CEM} is derived from the constant-rate region of cell survival curves where the slope is $D_0(T)$ and where the surviving fraction is $C(\tau)/C(0)$, the relationship between *CEM°43* and Ω is deceptively simple, that is

$$\boldsymbol{\Omega = \frac{CEM43}{D_0(43)}} \tag{3.4}$$

PHYSICAL MODEL FOR THE PRESENT RESEARCH

The tissue ablation model developed here is based on a sequence of thermal and fluid flow processes that globally obey Newton's Second Law for fluid flow, the First Law of Thermodynamics for phase change, the Fourier Law of Heat Conduction, and the Pennes Bioheat Model. The delivered vapor is at an intrauterine gauge pressure of 42mm Hg and at a corresponding saturation temperature that is 101.51°C. The uterine surface temperature is below that of the vapor, giving rise to sustained condensation along the walls of the uterine lining.

The model developed for the aforementioned processes has built-in intelligence in that the rate of utilized steam flow is auto-regulated by the rate of condensation and the rate at which heat penetrates the uterine tissue. This auto-regulation is the result of the tight interconnection of all of the involved physical processes. If the rate of delivered steam flow exceeds the auto-regulated value, it will leave the uterine cavity through the provided outlet. Because the rate of utilized steam flow is auto-regulated, the pattern of vapor motion is not explicitly considered within the model.

The change of phase from vapor to liquid deposits a condensate film on the uterine surface. For each kilogram of steam that is condensed, approximately 2250 kJ of thermal energy is liberated. The thickness of the film grows with the passage of time. Since the liberation of latent heat occurs at the vapor-liquid interface of the growing film, the heat must first pass through the liquid film before it reaches the uterine surface. The thickening of the condensate film creates a concomitant increase of the resistance to trans-film heat flow. Another impact of the increased thermal resistance is an increase of the temperature drop across the film. As a consequence, the uterine surface temperature is below both the condensation temperature of the vapor and the boiling-point temperature of the fluids that are contained in the uterine tissue.

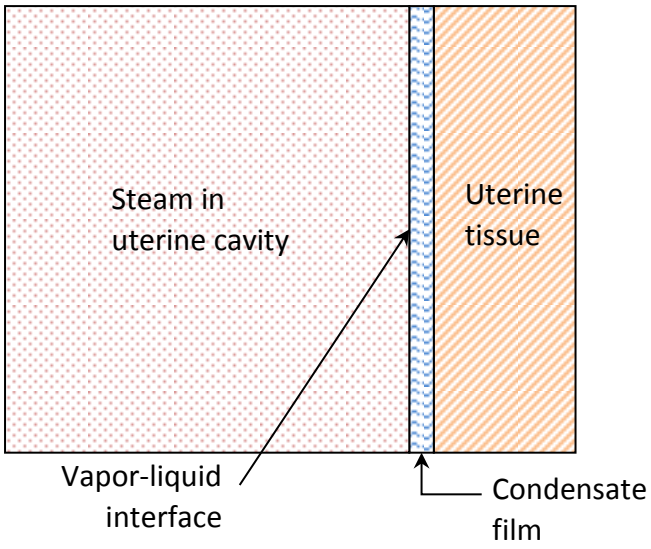

Figure 3.9 – Illustration of condensate film on uterine lining

The thermal energy deposited on the uterine wall by condensation penetrates the uterine tissue by two transport mechanisms. One of these is heat conduction, which is a molecular-level process that is indigenous to all media. Human tissue is not a good conductor of heat. The thermal conductivity of uterine tissue varies with several parameters including, among others, the water content in the tissue, [42]. For the current work, it is appropriate to use a value of approximately 0.5 W/m-°C. It is of the same order as biomedical fluids, as can be seen in Table 3.1.

Table 3.1 – Thermal conductivity values of common relevant substances

Material	**Thermal Conductivity (W/m-°C)**
Uterine tissue	0.5 [43]
Blood	0.49 [44]
Liquid water	0.63 [45]

A second heat transport mechanism is blood perfusion, which is a seepage-like process. Heat is carried by the perfusing blood, also called the “heat sink” effect. Living tissue experiences blood perfusion, but necrotic tissue does not. In partially necrosed tissue, the rate of perfusion is significantly diminished. These in-vivo processes are brought together in the bioheat equation.

Based on a careful evaluation of the biomedical literature, uterine cavity lengths of 26, 46, and 86 mm were selected for the numerical simulations. With the assumption of an average cervical length of 34 mm, these cavity lengths correspond to overall uterine lengths of approximately 60, 80 and 120 mm.

GOVERNING EQUATIONS

The physical processes that were described in the foregoing are governed by universally accepted conservation laws. The fluid flow and thermal energy transport in the vapor that floods the uterine cavity and in the condensed liquid must respectively obey Newton's Second Law, the law of mass conservation, the First Law of Thermodynamics, and the phase equilibrium law for water substance. For laminar flow, they are

Conservation of mass

$$\frac{\partial u_i}{\partial x_i} = 0 \tag{3.5}$$

Newton's Second Law for a fluid experiencing laminar flow

$$\rho \frac{\partial u_j}{\partial t} + \rho \left(u_i \frac{\partial u_j}{\partial x_i} \right) = -\frac{\partial p}{\partial x_j} + \frac{\partial}{\partial x_i} \left(\mu \frac{\partial u_j}{\partial x_i} \right) \; j = 1, 2, 3 \tag{3.6}$$

First Law of Thermodynamics

$$\frac{\partial T}{\partial t} + \left(u_i \frac{\partial T}{\partial x_i} \right) = \frac{\partial}{\partial x_i} \left(\left(\frac{k}{\rho c_p} \right) \frac{\partial T}{\partial x_i} \right) \tag{3.7}$$

In these equations:

u_i – velocity components of the flowing fluid (m/s)

T – temperature (°C)

p – pressure (kg/m^2)

ρ – fluid density (kg/m^3)

μ – dynamic viscosity (kg/m-s)

k – thermal conductivity (W/m-°C)

c_p – specific heat (J/kg-°C)

x_i – coordinates

t – time (s)

In addition to the foregoing equations, the phase change must occur in accordance with the liquid-vapor saturation curve for water substance. That curve is often referred to as the Clausius-Clapeyron relation and is presented in Figure 3.10. The figure shows the phases in question and the pressure and temperature coordinates which define those phases. Also shown is a point which indicates the state at which the vapor enters the uterine cavity. It can be seen that the vapor is slightly superheated.

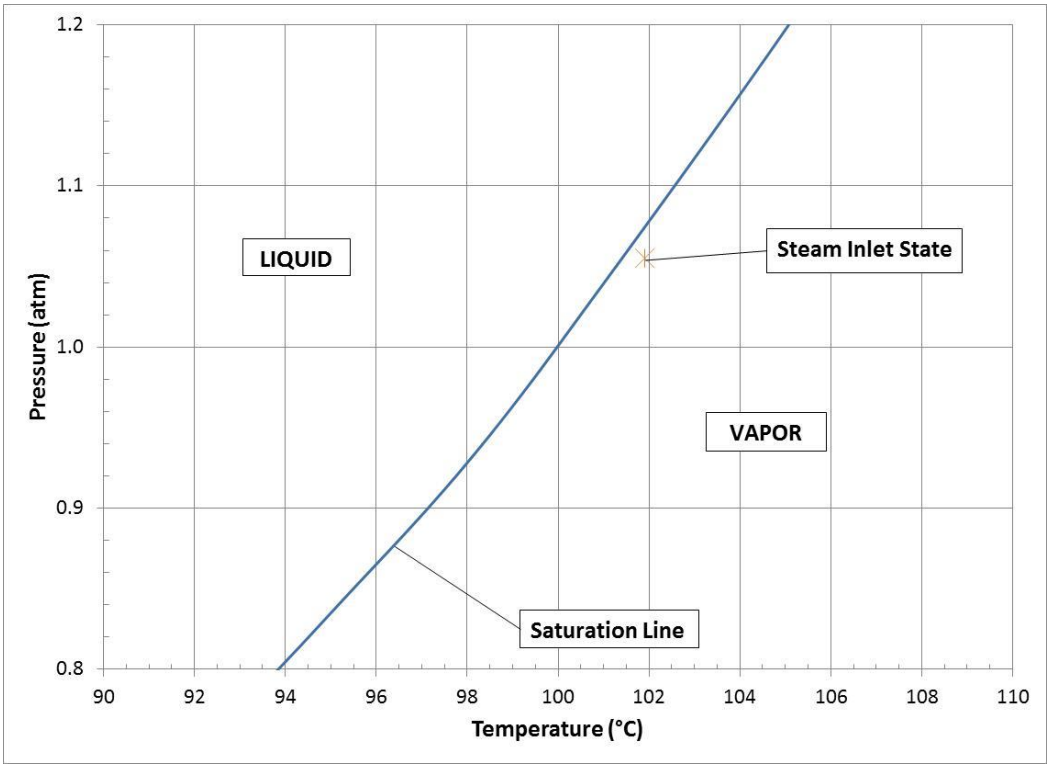

Figure 3.10 – Liquid-vapor saturation curve for water substance and a point corresponding to the inlet state of the vapor.

The water substance that enters the uterine cavity is a pure vapor whose temperature is 101.9°C and whose absolute pressure is 802 mmHg. The saturation temperature corresponding to this pressure is 101.5°C. Therefore, the vapor is slightly superheated. When the vapor contacts the uterine wall, whose initial temperature is on the order of 37°C, its temperature drops while the near-wall pressure drops slightly. In terms of the saturation diagram, the initial near-wall state is vapor. The slight near-wall pressure drop serves as a *defacto* pump in that it creates a pressure difference between the bulk vapor and the near wall. The condensate flow is governed by Eq. (3.5) and (3.6) with appropriate fluid properties. Similarly, the transfer of thermal energy in the liquid film obeys Eq. (3.7), but with the properties of the liquid.

The boundary conditions for the fluid flow represented by Eqs. (3.5) and (3.6) are the well-established no-slip and impermeability that prevail at all solid surfaces. On the other hand, the thermal boundary condition for the energy equation Eq. (3.7) is expressed by continuity of temperature and heat flux at all interfaces.

The transfer of thermal energy within the tissue was modeled by the Pennes Bioheat equation [46], which is a specific form of the First Law of Thermodynamics. This equation is the most widely used for bioheat processes in tissue. Many more detailed bioheat equations have been proposed, but they universally suffer from the fact that they contain unknown constants that are additional to the few that appear in the Pennes model. Because of this situation, the use of bioheat models other than that of Pennes is a rare occurrence.

The form of the Pennes Bioheat equation that was utilized for the tissue comprising the uterine wall is:

$$\left(\rho c_p\right)_{tissue}\frac{\partial T_{tissue}}{\partial t}=\frac{\partial}{\partial x_i}\left(k_{tissue}\frac{\partial T_{tissue}}{\partial x_i}\right)+\omega\left(\rho c_p\right)_{blood}\left(T_{artery}-T_{tissue}\right)$$

$$+Q_{metabolic} \qquad (3.8)$$

In this equation, ω represents the volumetric flow rate of perfusing blood per unit volume of tissue, and $Q_{metabolic}$ is the volumetric rate of metabolic heat generation. The following values were used in the numerical simulation:

$\rho_{tissue} = 980\ kg/m^3$

c_p of tissue = 3800 J/kg-K

k_{tissue} is a function of temperature = -0.00679368*T + 2.627 W/m-K

$(\rho c_p)_{blood} = 4.1 \times 106\ J/m^3\text{-}K$

$\omega = 0.0005\ s^{-1}$

$Q_{metabolic} = 500\ W/m^3$

COMPUTATION METHODOLOGY

A finite-volume approach was used to implement the numerical simulation utilizing the commercially available software package ANSYS CFX, version 14.0. The geometry was modeled as being axisymmetric to help conserve computational resources while maximizing nodal density. The several interlocking physical processes are all *unsteady* and vary throughout the volume of the uterine cavity and its enveloping tissue wall. To capture the time-dependent response, the solution was run as a transient covering the 140-second steam treatment. The time span was divided into 2800 time steps, giving a time step of 0.05 seconds.

In the case of the smallest uterine cavity (26 mm), the numbers of nodes needed were 1,708,700 and 250,900 for the tissue and fluid regions respectfully (1,959,600 nodes in total). The placement of the nodes was performed in a manner that resulted in significantly higher nodal densities closest to the uterine wall. This increased nodal density is required to achieve accurate results for the steam condensation and temperature distributions through the immediate area tissue.

APPLICATION OF A NECROSIS CRITERION

The numerical simulations provide spatial variations of the temperatures throughout the entire solution domain for all times between the initiation of the therapy and 140 seconds thereafter. At any selected spatial location, a complete time history is available. Consequently, the information needed to assess the attainment or non-attainment of necrosis at that location is at hand.

As was discussed in detail earlier, the most widely accepted means of assessing the state of tissue ablation subjected to elevated temperatures is Eq. (3.3). That criterion is widely termed the Henriques-Moritz integral criterion. The integral that appears in Eq. (3.3) takes account of both the instantaneous magnitude of the temperature and the times over which the varying temperature prevail. When Eq. (3.3) is specialized to the time integral that is relevant to the present therapy, there results:

$$\Omega = A \int_{t=0}^{t=140\ sec} e^{-\Delta E/RT}\, dt \qquad (3.9)$$

In this equation, the symbols *A, ΔE, R,* and *T* respectively denote the pre-exponential constant, the activation energy, the universal gas constant, and the instantaneous temperature. The symbol *t* denotes time. The values of *A* and Δ*E* are specific to the type of tissue involved which, for uterine tissue, are 3.10×10^{98} s^{-1} and 6.27×10^{8} J/kmole respectively [47]; the value of *R* is 8.314 kJ/kmole-K. As noted earlier, the threshold of irreparable tissue damage corresponds to Ω = 0.53 and that total necrosis is achieved for Ω = 1.

The methodology employed for the evaluation of Eq. (3.9) was initiated by the selection of a specific location on the surface of the uterine cavity. Along a line perpendicular to the surface at that location and in the direction beneath the surface, a set of points were selected, and the Ω integral was evaluated at each of these points. As expected, very large values of Ω were encountered near the surface of the uterine cavity. At points situated at increasing depths beneath the

surface, the values of Ω decreased monotonically. When the values of Ω = 0.53 and 1.0 were encountered, note was made of the corresponding locations and this information was stored for later presentation.

SIMULATION RESULTS

PREDICTED NECROSIS DEPTHS

Results for the depth of necrosis have been extracted from the numerical simulations at four critical locations along the circumference of the uterine cavity. Those locations and their designations are illustrated in Figure 3.11. The results for the three selected geometric lengths of uterine cavities are displayed in

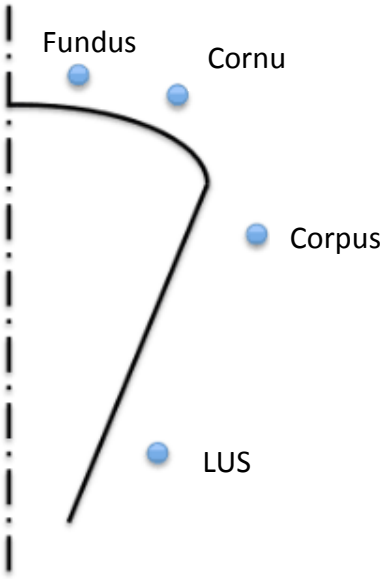

Figure 3.11 – Illustration of the four critical locations and their naming convention

Figures 3.12-3.14, respectively for lengths of 26, 46, and 86 mm. With the assumption of an average cervical length of 34 mm, these cavity lengths correspond to total uterine lengths of approximately 60, 80 and 120 mm.

Figure 3.12 displays necrosis depths for the cavity length of 26 mm. Inspection of the figure indicates depths ranging from 3.2 to 4.1 mm. It may be noted that the necrosis depths encountered along the long wall of the cavity are slightly

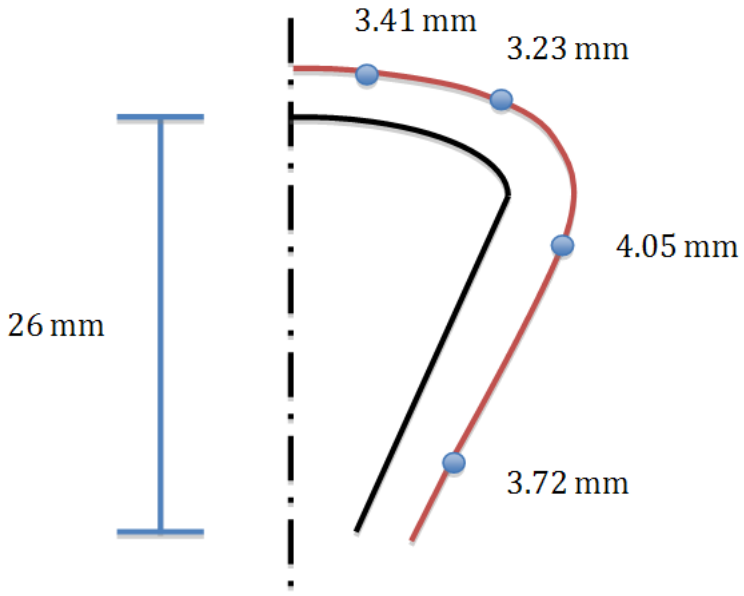

Figure 3.12 - Simulation-based necrosis depths (Ω = 1) for a uterine cavity of 26 mm in length (corresponding to total uterine length of 60 mm). The numerical values indicated in the diagram correspond to necrosis depths achieved with a 140-second treatment.

greater than those at the end wall (i.e., the fundus). These results will be compared to experimental data shortly.

Necrosis depth results for cavity lengths of 46 and 86 mm are presented in Figs. 3.13 and 3.14, respectively. The numerical values of the depths are in the same range for all three of the investigated lengths, and, generally, the same trends hold for all.

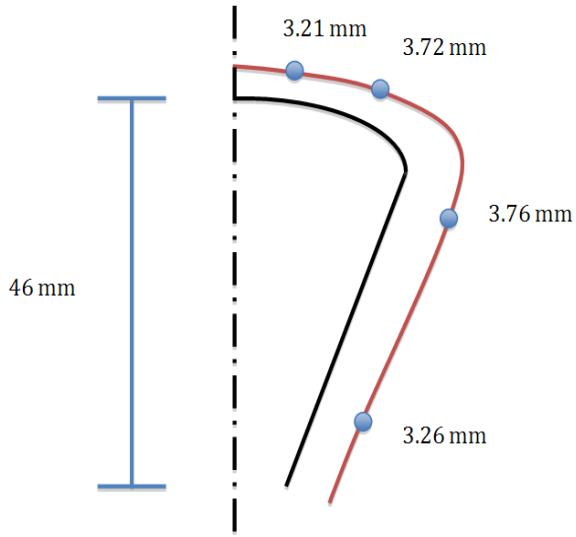

Figure 3.13 - Simulation-based necrosis depths (Ω = 1) for a uterine cavity of 46 mm (corresponds to 80 mm total uterine length) in length. The numerical values indicated in the diagram correspond to necrosis depths achieved with a 140-second treatment.

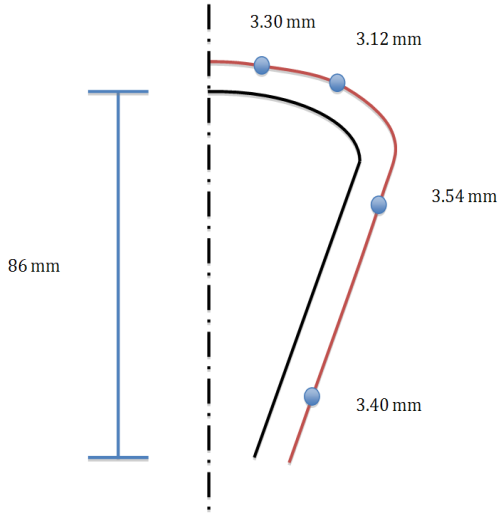

Figure 3.14 - Simulation-based necrosis depths (Ω = 1) for a uterine cavity of 86 mm in length (corresponding to 120 mm total uterine length). The numerical values indicated in the diagram correspond to necrosis depths achieved with a 140-second treatment.

The results from the numerical simulations will now be compared with those from experiments [48]. These experiments were performed on patients who had agreed that hysterectomy was the more appropriate treatment for their situation. Each of the treated uteri was carefully evaluated immediately upon the completion of the hysterectomy. Table 3.2 has been created to bring together the results from the simulations and those from experiment. Note that the experimental data were not classified according to the length of the uterine cavities.

The table is constructed in two parts. The upper part displays results from the numerical simulations, separately for the three selected uterine lengths. For each of the lengths, necrosis depths are indicated at the four critical locations identified earlier. To facilitate comparisons with the experimental data, for which only average values over the patient population are available, the numerical values from the simulations were also averaged at each of the critical locations. The lower portion of the table exhibits the experimental data, separately categorized as the average maximum values and the average minimum values of the measured necrosis depths.

Not unexpectedly, the simulation-based predictions are lower than the average of the maximum values from the experiments. These deviations are moderate for the Fundus, Cornu and Corpus locations. On the other hand, the deviation in evidence at the LUS location is considerably greater than that at the other three locations. This outcome cannot be presently definitively explained. However, a comparison of the average maximum and average minimum values of the experimental data reveals that the greatest differences occur at the LUS location. This finding suggests that large variations among individual measurements existed at that location, thereby diminishing concerns about the large deviation between the simulation predictions and the experimental data there.

Table 3.2 – Comparison of necrosis (Ω = 1) depth results from numerical simulation to experimental (pathology) results [48]

	Case Description	Necrosis Depth (mm) (from Figs. 3.12-3.14)			
		Fundus	**Cornu**	**Corpus**	**LUS**
Simulation Results	**26 mm**	3.41	3.23	4.05	3.72
	46 mm	3.21	3.72	3.76	3.26
	86 mm	3.30	3.12	3.54	3.40
	Average for all cavity lengths	3.31	3.36	3.78	3.46
Pathology Results Average Ablation		3.21	2.82	3.77	3.82

The numerical simulations also provided tissue depths at which the tissue damage criteria Ω = 0.53 were encountered. A comparison of the tissue depth results for these two different Ω values from the numerical simulations is presented in Table 3.3. For completeness, the table also includes the experimental data.

Table 3.3 – Comparison of numerical predictions of tissue depth corresponding to Ω = 0.53 and 1 for treatment duration of 140 seconds [48]

Cavity Size	Necrosis Criteria (Ω)	Necrosis Depth at Specified Circumferential Location (mm)			
		Fundus	Cornu	Corpus	LUS
26 mm	0.53	3.53	3.48	4.25	3.82
	1.0	3.41	3.23	4.05	3.72
46 mm	0.53	3.33	3.95	3.97	3.37
	1.0	3.21	3.72	3.76	3.26
86 mm	0.53	3.42	3.34	3.77	3.61
	1.0	3.30	3.12	3.54	3.40
Average	0.53	3.43	3.59	4.00	3.60
	1.0	3.31	3.36	3.78	3.46
Pathology Results Average Ablation		3.21	2.82	3.77	3.82

Inspection of the table shows that for all cases, the Ω = 0.53 criterion was encountered at a slightly greater depth than was the Ω = 1.0 metric. The differences between the respective depths are generally small, with the largest differences being on the order of 0.2 mm.

Inasmuch as the temperature wave that penetrates the uterine lining does not necessarily cease its penetration at the moment when the therapeutic treatment ceases, the simulations were extended from the end of the therapy (140 seconds) to 400 seconds, adding an additional 260 seconds. The conditions of irreparable tissue damage, or complete necrosis, are caused not only by the elevated temperatures, but also the duration of time that the tissue experiences the elevated temperature. Necrosis might occur after being at an elevated

temperature T_1 for a duration of X seconds, but it is possible to achieve necrosis of the same tissue after being at a lower temperature T_2 where $T_2 < T_1$ for a longer period of time, Y seconds such that Y > X.

Table 3.4 – Comparison of necrosis depth results from numerical simulation, using the Ω = 0.53 criterion, to pathology results [48]

Cavity Size	Treatment Time (sec)	Necrosis Depth at Specified Location (mm)			
		Fundus	Cornu	Corpus	LUS
26 mm	140	3.53	3.48	4.25	3.82
	400	4.07	3.83	4.68	5.57
46 mm	140	3.33	3.95	3.97	3.37
	400	3.83	4.35	4.55	3.85
86 mm	140	3.42	3.34	3.77	3.61
	400	3.93	3.74	4.31	4.09
Averages	140	3.43	3.59	4.00	3.60
	400	3.94	3.97	4.51	4.50
Pathology Results Average Ablation		3.21	2.82	3.77	3.82

Table 3.4 shows that the numerically predicted depths of necrosis corresponding to the end of the extended treatment are much closer to the average maximum ablation depths from the experiments than are those encountered at the conclusion of the period of actively applied therapy. This outcome suggests that during the time period between the end of the therapy proper and the extraction of the uterus, thermal penetration continued.

Information similar to that conveyed by Table 3.4 but relevant to the Ω = 1 criterion are presented in Table 3.5.

Table 3.5 – Comparison of necrosis depth results from numerical simulation, using the Ω = 1 criterion, to pathology results [48]

Cavity Size	Treatment Time (sec)	Necrosis Depth at Specified Location (mm)			
		Fundus	Cornu	Corpus	LUS
26 mm	140	3.41	3.23	4.05	3.72
	400	3.83	3.59	4.45	5.34
46 mm	140	3.21	3.72	3.76	3.26
	400	3.65	4.04	4.33	3.68
86 mm	140	3.30	3.12	3.54	3.40
	400	3.75	3.52	4.10	3.82
Averages	140	3.31	3.36	3.78	3.46
	400	3.74	3.72	4.29	4.28
Pathology Results Average Ablation		3.21	2.82	3.77	3.82

Once again, the average necrosis depths for all three cavity lengths are compared in the table with the average maximum values from the experiments. In general, there is very good agreement between the simulation-based results and the experimental values. The only deviation from this conclusion is at the LUS location. The justification for that deviation has already been set forth earlier.

To complete the presentation of the necrosis depth information, Figures 3.15-3.17 were prepared. These figures are the counterparts of Figures 3.12-3.14, except that the earlier figures corresponded to Ω = 1.0 and the current figures are for Ω = 0.53. These figures are for the termination of the application of the treatment, 140 seconds. The trends in evidence in Figures 3.15-3.17 mirror those already identified in Figures 3.12-3.14.

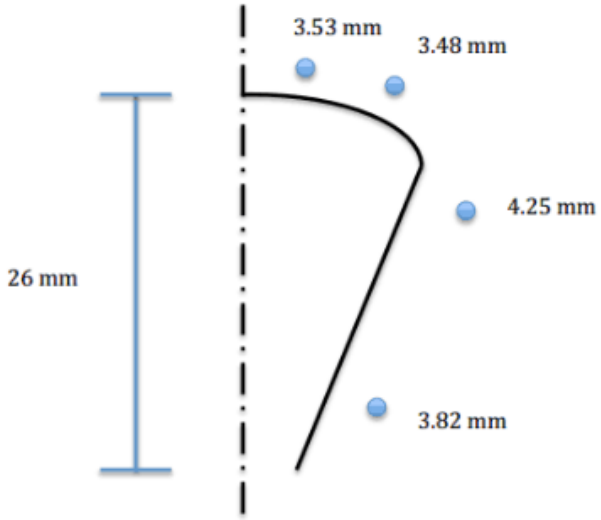

Figure 3.15 - Simulation-based irreparable tissue damage (Ω = 0.53) depths for a uterine cavity of 26 mm (corresponds to 60 mm uterine length) in length. The numerical values indicated in the diagram correspond to tissue damage depths achieved with a 140 second treatment.

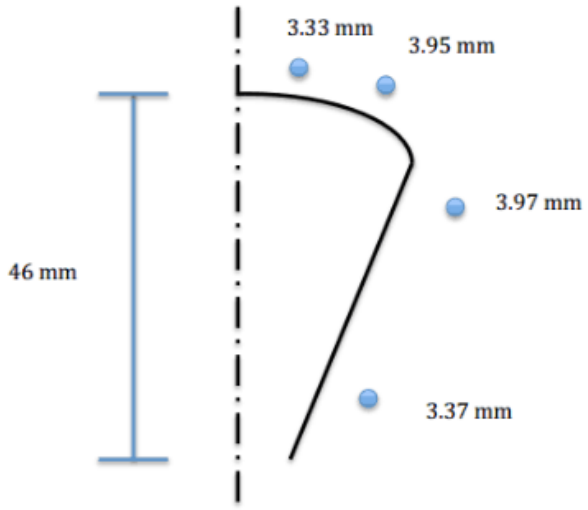

Figure 3.16 - Simulation-based irreparable tissue damage (Ω = 0.53) depths for a uterine cavity of 46 mm (corresponds to 80 mm uterine length) in length. The numerical values indicated in the diagram correspond to tissue damage depths achieved with a 140 second treatment.

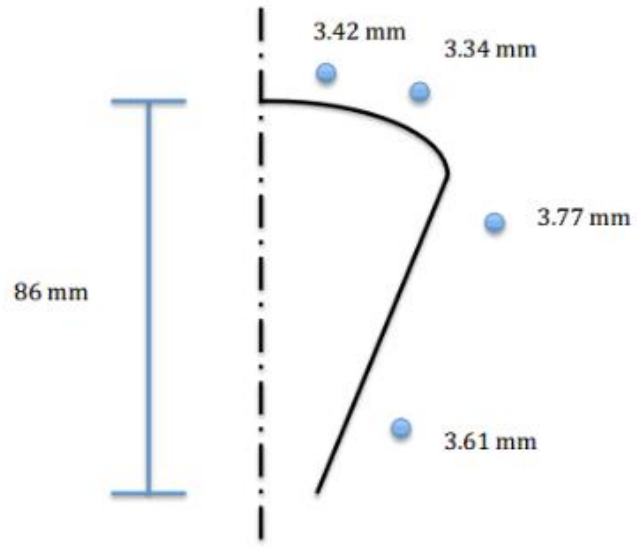

Figure 3.17 - Simulation-based irreparable tissue damage (Ω = 0.53) depths for a uterine cavity of 86 mm (corresponds to 120 mm uterine length) in length. The numerical values indicated in the diagram correspond to tissue damage depths achieved with a 140 second treatment.

TEMPERATURE DISTRIBUTIONS

Spatial temperature distributions will be presented from two points of view. The first is a display, by means of color contour diagrams, of the distribution of temperature throughout the uterine tissue at the termination of the treatment (140 seconds of vapor delivery). This information is conveyed in Figures 3.18-3.20 for the cavity lengths of 26, 46, and 86 mm (corresponding to total uterine lengths of 60 mm, 80 mm and 120 mm, respectively).

The colors that characterize the spatial temperature distributions are keyed to a legend appearing at the left of the respective figures. To facilitate easy appraisal of the results, the range of temperatures is the same for all color legends.

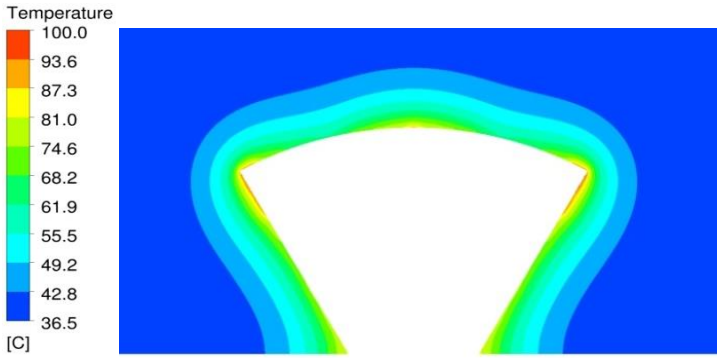

Figure 3.18 - Simulation-based distribution of temperature throughout the uterine tissue at the termination of the 140-second treatment for a cavity of 26 mm in length (total uterine length of 60 mm).

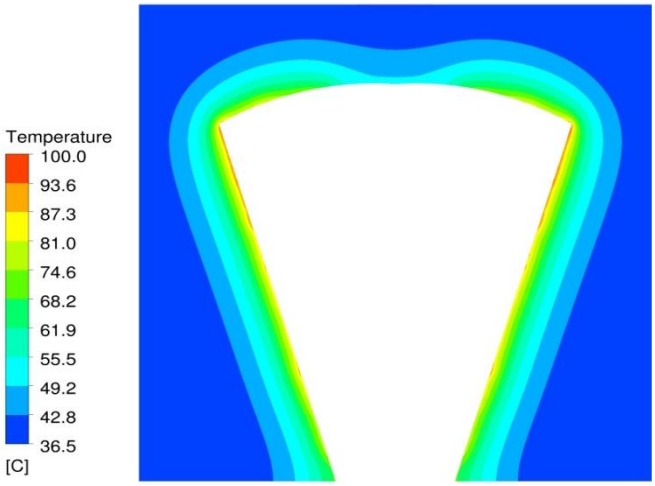

Figure 3.19 - Simulation-based distribution of temperature throughout the uterine tissue at the termination of the 140-second treatment for a cavity of 46 mm in length (total uterine length of 80 mm).

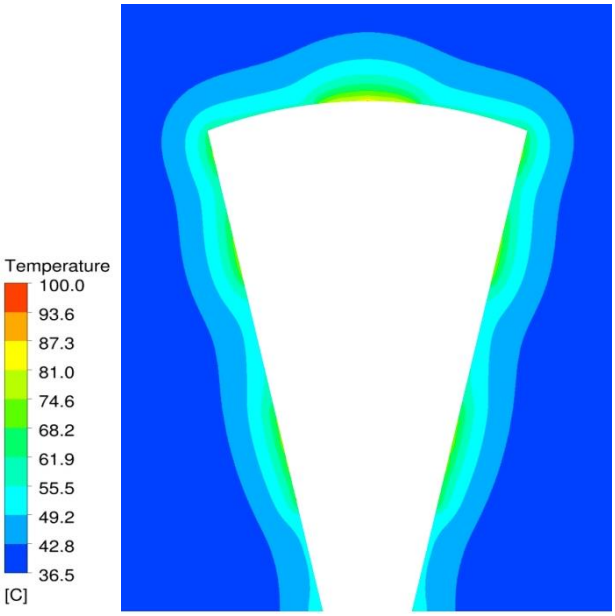

Figure 3.20 - Simulation-based distribution of temperature throughout the uterine tissue at the termination of the 140-second treatment for a cavity of 86 mm in length (total uterine length of 120 mm).

Inspection of the figures reveals a general similarity in the temperature results for the three cavity lengths, with small differences in detail. The shorter cavities experience somewhat higher temperatures than their longer relative as witnessed by the appearance of the orange and yellow colors at the upper end of the cavity. Furthermore, it is clear that the temperature distribution patterns are affected by the steam distribution along the surface of the cavity wall. Clearly, the intermediate-length cavity experiences a highly uniform steam delivery. In contrast, the steam delivery is evidently non-uniform for the longest of the cavities.

The second mode of spatial temperature-distribution presentation is in terms of a graph, Figure 3.21. In the figure, the temperature is plotted on the vertical axis while the distance from the cavity surface is represented on the horizontal axis. There are several curves which are parameterized by times ranging from 15 to 140 seconds. At any fixed time, the temperature is seen to decrease

monotonically with increasing distance from the cavity surface. Further inspection reveals that the most rapid decrease of the temperature with depth occurs at the shorter times. It can be seen from the figure that the temperatures never exceed the boiling temperature that corresponds to the pressure within the cavity. For increasing times following the initiation of the treatment, the tissue temperatures display an increasing trend.

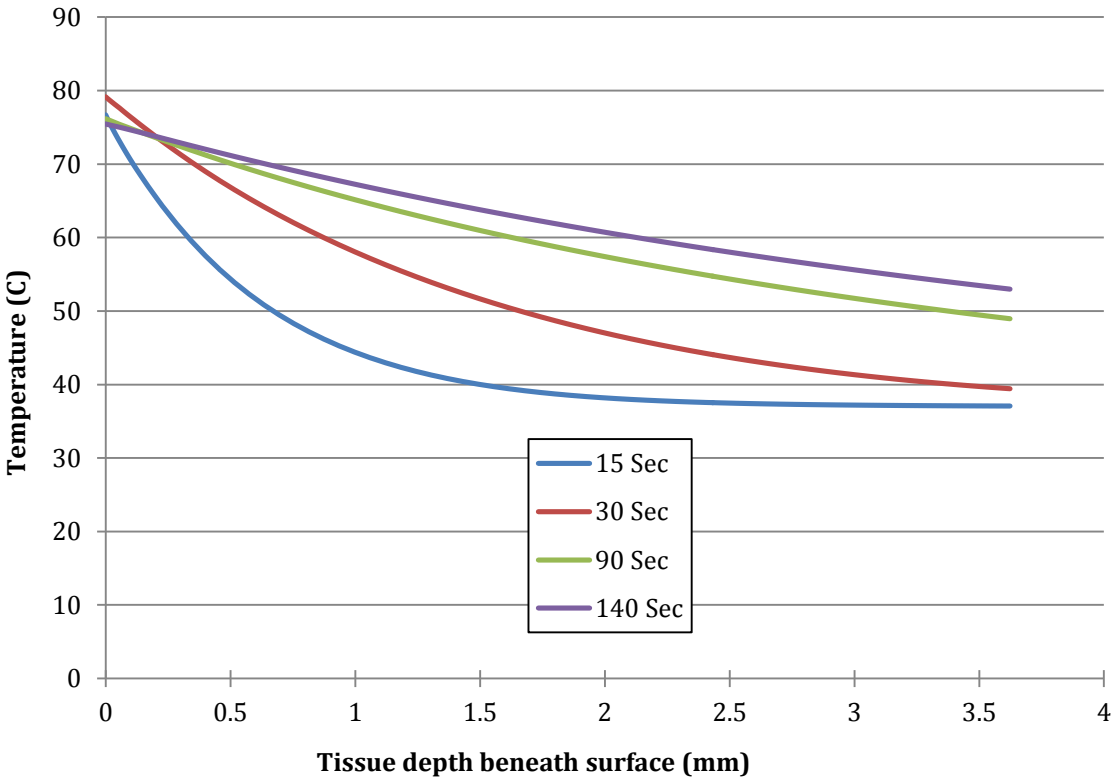

Figure 3.21 - Typical temperature distributions as a function of tissue depth beneath the cavity surface for various times during the therapy application.

Heat transfers through the uterine tissue by means of conduction, with a rate defined by the thermal conductivity of the tissue, and heat carried by blood perfusion, as illustrated in Eq. (3-8). The rate of heat transfer due to blood perfusion is dependent upon the amount of necrosis in the tissue. These factors

ultimately define the rate at which the temperature wave travels through the tissue over time. To illustrate this phenomenon, three points were selected in the uterine tissue at which the temperature as a function of time is plotted in Figure 3.22. The three points are all located half-way up the side of the uterine wall, and 1, 2 and 3mm deep into the tissue, orthogonal from the tissue-fluid interface. The Figure shows that the temperature rise starts at a later time, and rises at a slower rate as the distance from the uterine wall is increased.

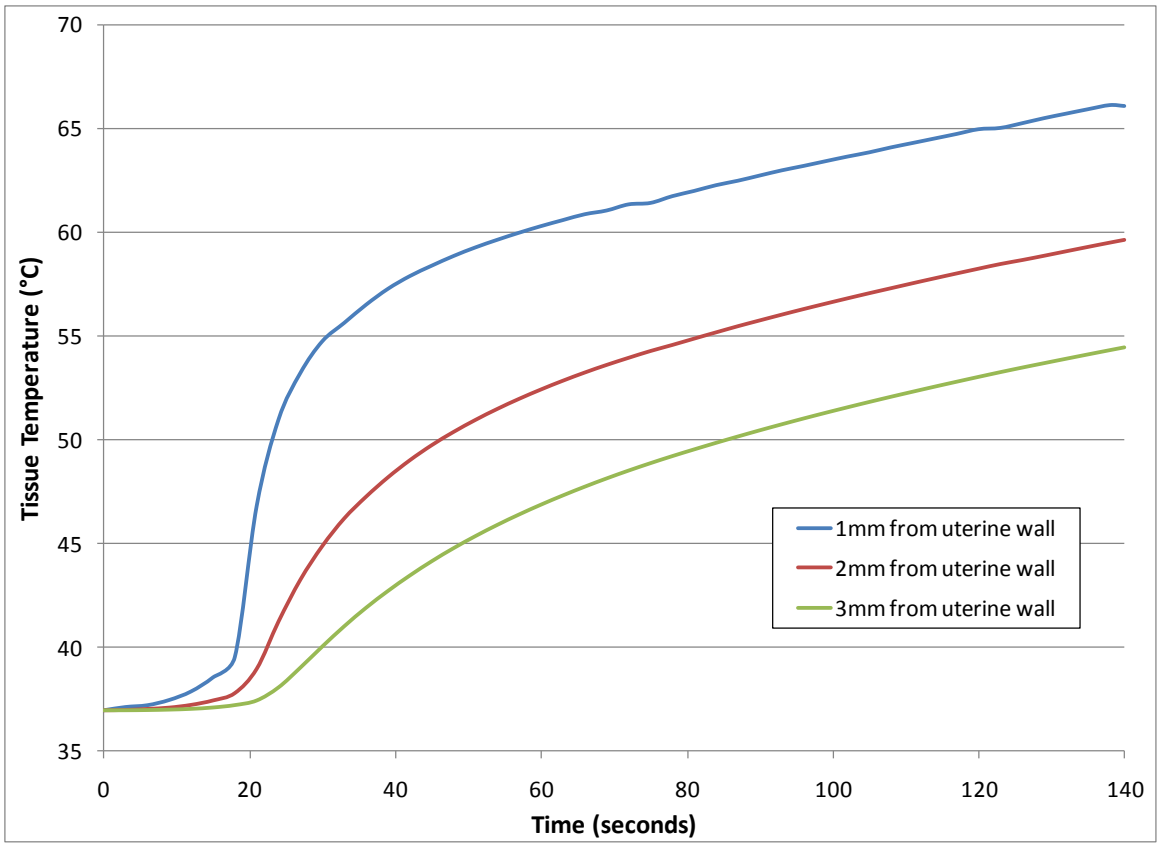

Figure 3.22 – Temperature of the uterine tissue at various distances from the uterine wall as a function of time.

CONCLUDING REMARKS

A numerical simulation model, implemented fully independently of clinical data, has demonstrated the efficacy of using water vapor as a means for treating menorrhagia. The model is based on first principles encompassing Newton's Second Law, the First Law of Thermodynamics for energy transport and phase change, the Clausius-Clapeyron relationship for phase equilibrium, the conservation of mass, Fourier's Law of heat conduction, and the Pennes Bioheat Equation.

The thermal energy needed for creating elevated temperatures in the tissue within the uterine cavity was provided by the latent heat of condensation of the steam. The rate of steam utilization is auto-controlled by the intimate interactions of the participating physical processes. Any delivered steam in excess of that needed for the therapy is vented outside the uterine cavity through the vapor probe.

The numerical simulations provided highly detailed information for the temporal and spatial distributions of temperature in the tissue that bounds the uterine cavity. This information was post-processed by means of the well-established Henriques-Moritz thermal damage integral. The values of this integral constitute a metric for establishing both the onset of irreparable tissue damage and the attainment of complete necrosis.

The numerical simulations were carried out for two time durations following the initiation of the therapy. One of these durations, 140 seconds, corresponds to the period during which the steam is being actively supplied. To take account of temperature spreading throughout the tissue subsequent to the cessation of the steam supply, the simulations were extended to 400 seconds. The necrosis depths corresponding to the extended time duration were found to be slightly greater than those for the applied therapy period.

The necrosis depths corresponding to these operating conditions were compared to available experimental information. The experimental results were obtained from post-inspection of extracted uteri which had been previously subjected to the vapor-based necrosis treatment. The extraction of the uteri was based on physicians' opinions that the dysfunctional condition had gone beyond the point where the therapeutic process could make a difference. The patients had volunteered to serve as subjects for the evaluation of the therapeutic process knowing that their uteri would ultimately be removed. The experimental results were grand averages encompassing uteri of various dimensions and at various stages of dysfunction.

The numerically predicted necrosis depths were compared to the average values obtained in the experiments. In general, the agreement between the depths of necrosis obtained from the simulations and those from the experiments were highly satisfactory. Only at the LUS location were there sizable deviations. However, there is compelling evidence of substantial scatter of the experimental data at that location, so that the deviations between the simulation and experimental results are not a major issue.

CHAPTER 4 – DESIGN METHODOLOGY FOR DELIVERING A THERAPEUTIC DRUG IN PARTICULATE FORM

INTRODUCTION

The investigation to be described in this chapter is a continuation of the theme of fluid-mechanic-based therapies. The focus of this chapter is to develop a methodology for delivering therapeutic drugs that enter the human body either through the mouth or the nostrils. For the applications in question, the drug may be delivered either in particle or droplet form. The issue at hand is to be able to predict the trajectory of these discrete entities as they pass from their point of admission to their targets within the respiratory system. The prediction of these trajectories is highly complex, owing especially of the complicated geometries of the flow passages in question.

Since the issue at hand is experiencing increased current interest in the biomedical community and the pace of related research is accelerating, the literature review was focused on the very recent past. It appears that the present state of capability in the numerical modeling of the complex flow passages has been confined to the upper reaches of the respiratory system. To illustrate the nature of the current level of accomplishment with regard to the flow-configuration modeling of the upper respiratory system, Figure 4.1 is presented. Models of this type were employed in numerous numerical simulations such as those reported in [49-51]. As can be seen from the figure, the geometry is not only highly simplistic but does not extend into the highly complex lung region. The most recent publication relevant to the work of this chapter appeared in print

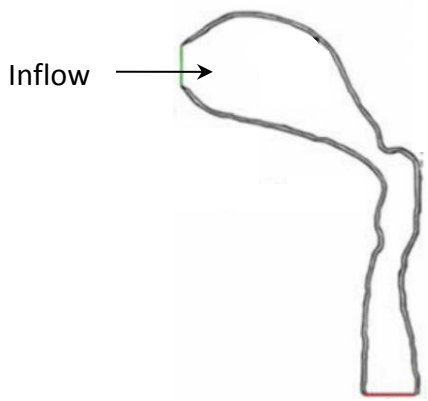

Figure 4.1 – Illustration of the state of the art of the modeling of the upper respiratory geometry

in October of 2013 [52]. That paper is a state-of-the-art review of modeling of drug delivery to deeper regions of the respiratory system. The review confirms the need for higher fidelity modeling than has appeared in the published literature. That outcome reinforces the motivation and the goals of the present investigation.

The objective of this work is to create a methodology suitable for application to problems of the type mentioned in the foregoing. It is well understood that the geometry of the respiratory system is not only complex, but also differs among individuals based on age, gender, and physical condition, among others. In this light, the task undertaken here is not specific to any of these categories. Rather, the development is carried out for a geometry of sufficient complexity to ensure the applicability of the developed methodology to a variety of complex geometries.

The fluid flow problem, without particulates, is very complex in its own right. The approach used here is to first solve for the fluid flow and subsequently take the particle motion into account. The investigation is performed for inhomogeneous particle-size distributions and is aimed at determining the sites at which the various particle sizes are collected.

PARTICLE TRANSPORT IN THE HUMAN RESPIRATORY TRACT

The path of particle motion in the human respiratory tract is determined by the presence of multiple physical phenomena. In any specific case, one such physical process may dominate over the others and determine the resultant trajectory and deposition location. In general practice, particle motions can be driven by gravitational, electrical, inertial, or diffusional forces. However, pharmaceutical particles are generally not charged and, therefore, there are no electrical forces to consider in the application of current study, and attention will be focused on the mechanical forces encountered. Furthermore, it has been well documented that an individual's breathing pattern has a profound effect on the delivery of a nebulized drug [53].

Particle transport by diffusion has the greatest effect when particle sizes are extremely small, typically less than 0.1 μm in diameter. Particles of this size interact with the surrounding carrier gas in a manner that is similar to collisions between particles. Each collision of a particle with a gas molecule changes the particle's direction of motion. This ultimately results in a random path that is independent of particle density. The observed randomness increases with time or decreasing particle size. As a result, it is reasonable to expect that diffusional deposition to govern in small airways such as those in the lung periphery [54].

At particle sizes larger than 0.1 μm, diffusion plays a smaller role in the transport path and other forces such as gravity and inertia play stronger roles. Gravitational forces play an increasing role with the increase of diameter, density, or time. Similar to the diffusion mechanisms, the time-dependence of gravitational transport suggests that it will be most prominent in areas of maximum residence time such as in small airways in the lung periphery.

Particle transport by means of inertia can be referred to as impaction. Particles of increasing size and density will have inertial displacement resulting from the

velocity of the air in the passageways. As the air velocity, particle size, or particle density increases, this transport modality becomes a more dominant factor in particle deposition patterns. In summary, the transport path of the smallest particles, termed ultrafine, is dominated by the diffusion mechanism. As particles get larger in size, gravitational forces contribute more to the particulate path. Of these larger particles of a given size, as the density increases, the inertial transport mechanism has a larger effect on the ultimate deposition patterns. Coincidentally, all particles with density, ρ, and diameter, d, which have an equivalent product of (ρd^2) are said to have the same aerodynamic behavior. In this instance, those particles will have the same gravitational displacement. Since both gravitational and inertial transport mechanisms are dependent on (ρd^2), they will have the same inertial transport as well. This approximation is not always appropriate. To be complete, the particle transport is influenced by slip force correction factors. The value of these correction factors depends on the relative difference of the particle's aerodynamic diameter and the mean free path of the surrounding carrier gas. In this application, it is determined that particles larger than 1 μm can neglect these correction factors with reasonable accuracy [54]. As such, these factors have not been included in the study at hand.

PARTICLE INERTIAL IMPACTION

Devices called particle impactors have been employed for many years to systematically sort particles which are entrained in an air stream based on their aerodynamic size. Such devices have been in favor due to their simple mode of operation and relative simplicity of design and manufacture. In the most simple view, an impactor directs a particle-laden airstream through a nozzle which discharges onto a target surface. The common principle under which all particle impactors operate is that high-inertia particles in an air stream will impact on the target surface, while lower-inertia particles will continue to follow the fluid streamlines [55]. A proper design of the impactor, including the diameter and

shape of the nozzle, the distance from the target surface, and the velocity of the airflow through the system will result in an accurate means of segregating particles based on their aerodynamic size. If the particles are of the same material, then the impactor will effectively sort the particles based on their physical size.

The aforementioned sorting process can be expanded to create more complex devices such as cascade or parallel impactors. In the case of a cascade impactor, the air stream is directed by means of a nozzle at a first target plate which is designed to collect particles that are larger than a specific size. Any particles that are smaller than this size will not impact the plate and will continue to follow the fluid stream. After passing the first collection plate, the flow and its cargo of particles will congregate in a plenum before being directed through a second nozzle, aimed at a second target plate. The second nozzle and its distance from the target plate will be different from that of the first. The design parameters of the second impactor will be such that it will collect particles that are smaller than those already collected at the first plate, but larger than the others in the air stream. This process can be repeated for many stages, resulting in an effective mechanism to separate the particles in an air stream into many different size ranges.

Figure 4.2 shows an example of a single-stage and a cascade-type particle impactor. The single-stage impactor is shown on the left side of the figure. In this configuration, the particles follow the streamlines through the nozzle and are directed towards the collection plate. Only particles of sufficient size, namely those that are larger than the design cutoff size, will impact and be collected on the plate. Any other particles that are smaller than the cutoff size will not have sufficient inertia to strike the plate, and will therefore continue out of the device with the exhausted air.

The illustration on the right side of the figure depicts a three-stage cascade impactor. In this configuration, the particle-laden airflow enters the device with particles of various sizes. The design parameters of the device are such that as the flow passes through the first nozzle and impacts on the plate (labeled Stage 3 in the figure), any particles larger than 10 µm will be collected. After passing through this stage, the air flow and remaining particles will continue out of this stage and enter the next stage (labeled Stage 2 in the figure). The design of the nozzle and the distance to the plate of Stage 2 are such that particles that are larger than 2.5 µm but less than 10 µm will impact and be collected. In a similar fashion, the air flow and remaining particles will next flow through the third nozzle, directed at the final collection plate (labeled Stage 1 in the figure). At this stage, particles that are larger than 1 µm but smaller than 2.5 µm will be collected. Finally, the airflow will exit the device, along with any particles that are smaller than 1 µm. In various commercially available devices, the flow will pass through a filter medium designed to collect the last remaining particles that are still in the flow stream.

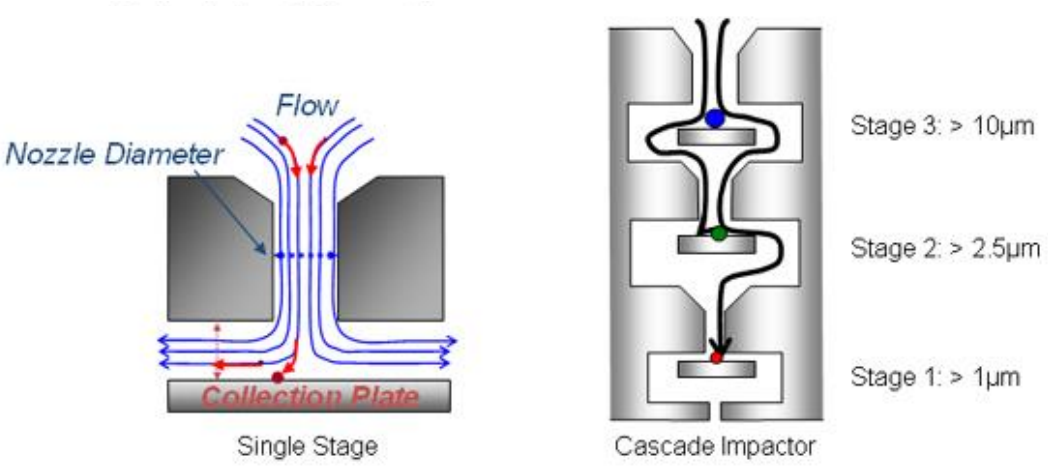

Figure 4.2 – Illustration of a single stage and cascade impactors.

Particle impactors are often classified by the size of particle they are designed to separate, commonly referred to as the cutoff size. The size is often designated

as d_{50} to indicate a 50% collection efficiency at the size noted as d. Figure 4.3 demonstrates an ideal and an actual cut-off curve for a typical impactor. A perfect impactor would behave according to the ideal curve, shown as a vertical line in the figure, whereby any particles larger than a given size would be collected and all particles smaller than the designated size would pass through. Real-world applications have various inefficiencies which prevent this ideal curve from occurring and instead give a performance curve like the actual one shown. The characteristic parameter of a given impactor is the size of the particles collected. The efficiency curve is based on the square root of the Stokes number (Stk), which is a dimensionless parameter comparing the particle's characteristic response time to the response time of the fluid [56]. The Stokes number is defined as:

$$Stk = \frac{\rho d^2}{18\mu}\frac{u_\infty}{L} \tag{4.1}$$

where

ρ – density of particle

d – diameter of the particle

u_∞ – velocity of the fluid

μ – viscosity of the fluid

L – representative length of the target surface

If the Stokes number is much less than one, the particle is tightly coupled to the fluid flow and has a low probability of being collected. If the Stokes number is large, then the particle is much less dependent upon the fluid flow, and its trajectory has much greater dependence on the other forces.

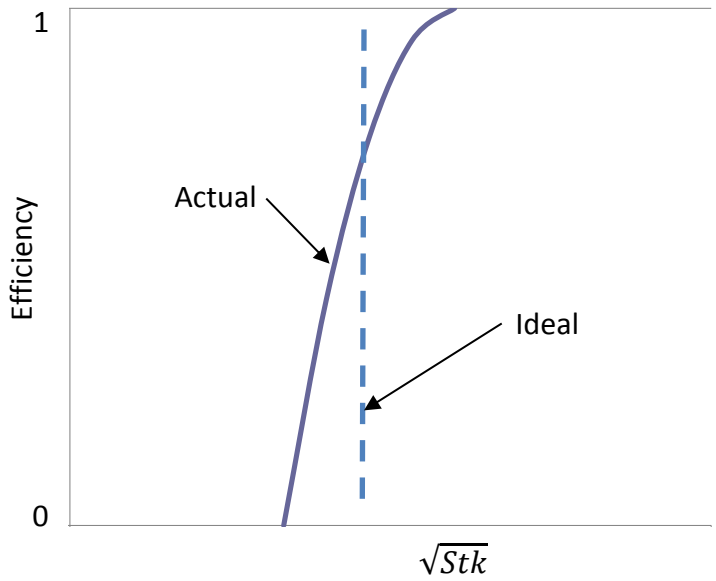

Figure 4.3 – Sample efficiency curve of particle impactor

PHYSICAL MODEL

Figure 4.4 depicts the flow model used here for the detailed study of the particulate flow. The objects that are encountered by the fluid along its flow path are shown in different colors to help distinguish one from the other. The system is comprised of potential collection zones connected together by bridging passageways. This configuration is believed to contain sufficient complexity to be suitable for the development of a methodology for treating drug delivery through the respiratory tree to the lungs.

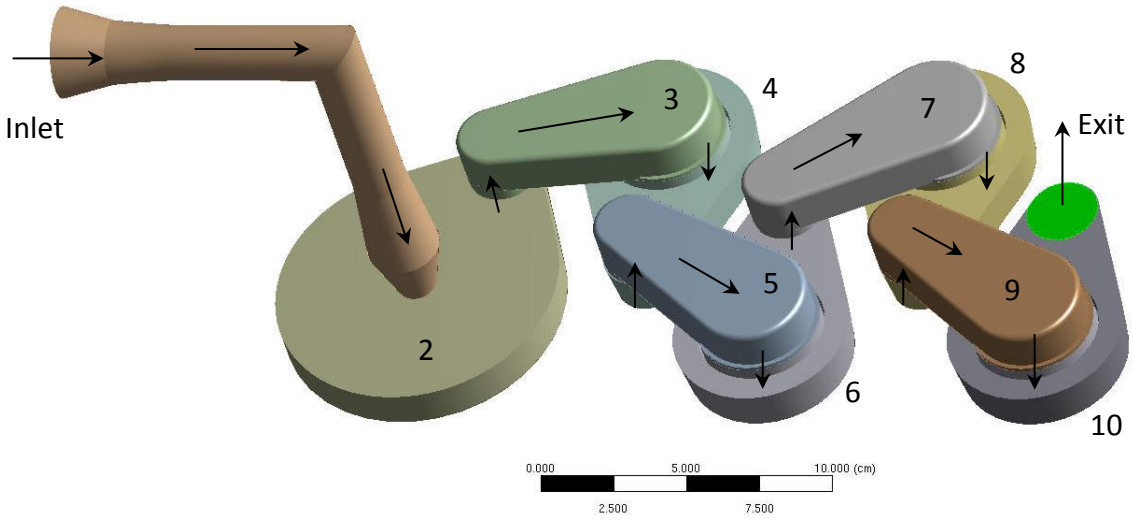

Figure 4.4 – Illustration of the flow pattern of study. Arrows are included to indicate the general direction of flow through the zones.

The model is arranged in such a manner that the lower zones, zones of even numbers 2 – 10, serve as potential particle collectors. The upper zones, those of odd numbers 3 – 9, serve as passageways that connect one collection zone to the next. The incoming air-particle mixture enters through the circular opening marked as number 1 in the figure. The flow continues through the snorkel-like tube assembly before discharging into the first potential collection zone marked as number 2 in the figure. The inlet snorkel may be viewed as an approximation of the mouth and throat in the human body.

Each successive collection zone is different from the previous one. As illustrated in Figure 4.5, the first potential collection zone, zone number 2, is of the simplest form whereby the incoming air-particle mixture enters through a single round opening in the top center and impinges on the flat bottom of the zone. Once inside the zone, the flow will recirculate until it exits through the round opening in the top, and immediately enters the connecting passageway

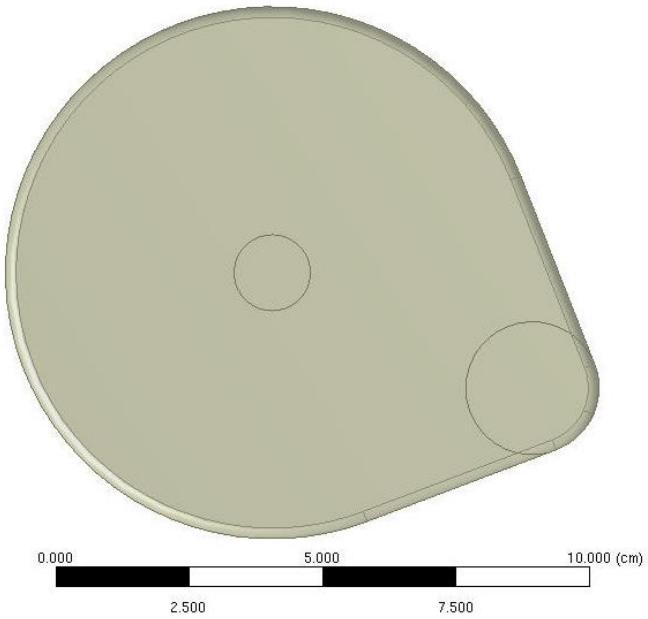

Figure 4.5 – Top view of collection zone number 2. All collection zones are of like size.

marked number 3. The air discharges from passageway number 3 and enters the second collection zone, labeled number 4, as seen in Figure 4.4.

The dimensions of the objects may be assessed by referencing the scale in Figure 4.5. As can be seen, the length of the first collection zone, labeled 2, is on the order of 10 cm. The height of each zone is approximately 1.5 cm. Figures 4.6 and 4.7 respectively depict the second and third collection zones, labeled numbers 4 and 6, and show the increasing number of round openings through which the fluid flows into the zone. The figures are shown to scale, making it easy to see that each of these openings is of smaller diameter than the opening through which the flowing medium entered into its predecessor collection zone. As the flow continues through the system, it enters each successive collection zone through a larger number of smaller-diameter openings than those of the previous collection zone. The final collection zone utilizes 152 holes whose diameter is 0.5 mm each. This pattern continues until the flow has

passed through all of the collection zones and finally exits through the round opening in the top of zone 10.

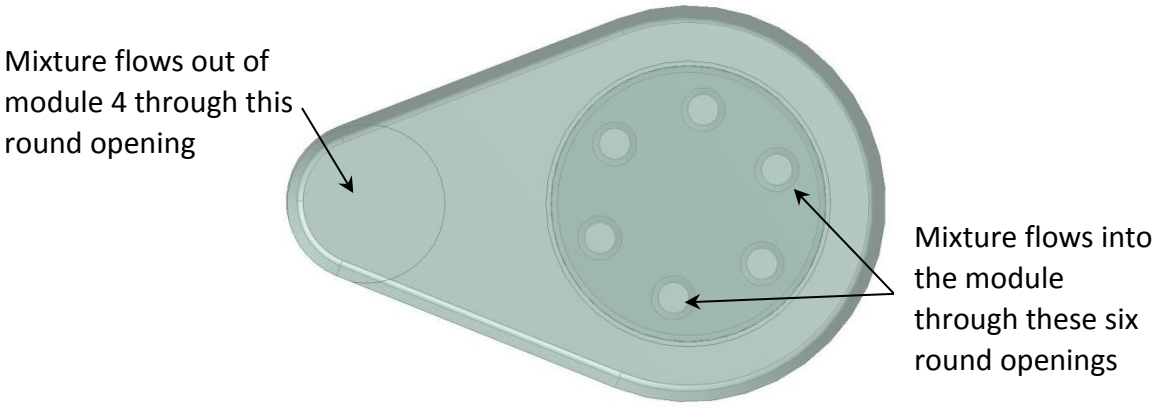

Figure 4.6 – Top view of collection zone number 4.

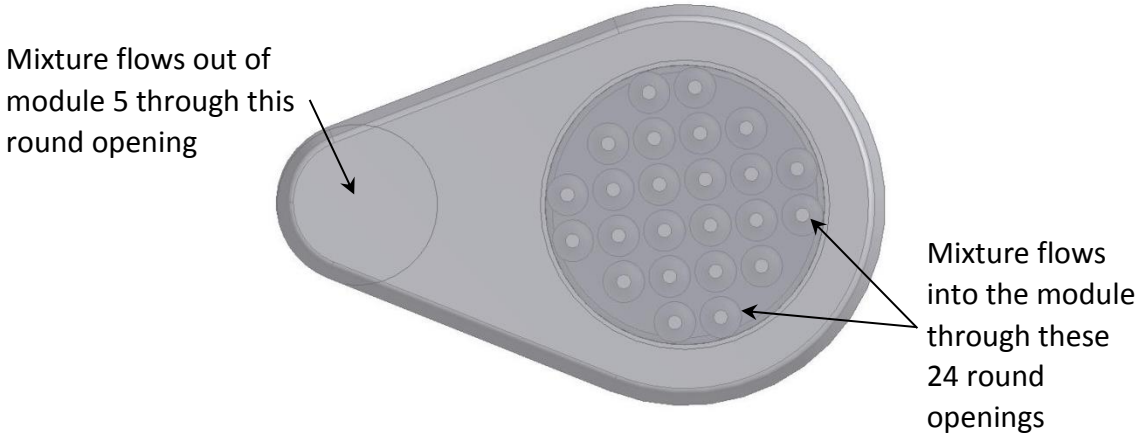

Figure 4.7 – Top view of collection zone number 6.

For the numerical simulations, a steady turbulent flow model was adopted. The inlet cross section, identified as station 1 in Figure 4.4, was designated as an opening. In computer parlance, an *opening* is a very weak boundary condition which enables the fluid to find its own direction, either to enter or leave. A further

constraint of this boundary condition is that the direction of fluid flow across the opening is prescribed to be perpendicular to the opening. In addition to the specification of the inlet boundary condition as an opening, it is also necessary to prescribe the pressure. The specified pressure is zero, so that all other pressures are regarded as gauge pressures. At the exit of the system, the mass flow rate was prescribed as 0.0005925 kg/second. This configuration corresponds to operation in the suction mode.

COMPUTATION METHODOLOGY

A finite-volume approach was used to implement the numerical simulation utilizing the commercially available software package ANSYS CFX, version 14.0. The geometry was meshed with a total of 4.75 million nodes. Such high numbers of nodes often prove to be very difficult to solve and obtain a reliable result. The method used in this work was to first reduce the geometry to contain only one collection zone and obtain the corresponding velocity solution. The geometry was then extended to include both the first and second zones. The use of velocity values determined in the prior solution provided reasonable velocity values to start the new solution. This methodology was continued, adding one module at a time until the final solution of five collection zones was reached. This approach was an innovation necessary to actually obtain convergence.

Due to the highly complex geometry, the numerical simulations were first conducted by solving for the fluid flow without any particles present in the simulation. Once an accurate velocity solution was obtained for all five collection zones, it was held constant and used for the next simulation which included the particles. The particles were included in the numerical simulation with a one-way interaction scheme. In this method, the presence of the particles has no influence on the fluid flow itself. This approach is reasonable considering the size and mass of the particles used are very small.

In addition to the large number of nodes, their deployment is a critical factor. The placement of the nodes was performed in a manner that resulted in significantly higher nodal densities closest to the bottom of each collection zone as well as through the various ports that carried the fluid into the collection zones. This increased nodal density is required to achieve accurate results for accurate fluid flow solutions and the particle deposition rates of interest.

The bottom surface of each collection zone was defined as having a coefficient of restitution equal to zero in both the perpendicular and parallel directions for particle impingement. This adoption was logic-based because the surface in question is coated with a sticky substance. Due to the aforementioned specification of the restitution coefficients, if any particle comes in contact with the bottom surface, it will stick to that surface and not continue through the system. All other surfaces of the collection zones and the surfaces of the connecting passageways utilized a coefficient of restitution equal to one and, therefore, allowed the particles to be reflected and continue through the system.

Particles of various distinct sizes were introduced into the system at the inlet. The largest size of particle used was 13 μm in diameter. The other particle sizes used were 8 μm, 5 μm, 3.1 μm, and 1.8 μm in diameter. The material used for the particles was aluminum, giving single particle mass values ranging from 3.1×10^{-12} to 8.3×10^{-15} kg. The particles were introduced at a rate of 100 per second of each size with an inlet velocity of 0.634 m/sec, matching that of the incoming airflow. A random spatial distribution of particles at the inlet cross section was used.

FORMULATION OF THE FLUID FLOW PROBLEM

To enable an unprejudiced approach to the fluid flow problem, a constitutive model was adopted which auto-determines the flow regime, encompassing laminar, intermittent, and fully turbulent. This multi-regime model is based on three interlocking sets of equations. The first set consists of the Reynolds-Averaged Navier-Stokes equations (RANS) and the equation of mass conservation. The RANS equations represent a first-stage introduction of turbulence into the traditional Navier-Stokes equations by means of the turbulent viscosity μ_{turb}.

The second set of equations is that which is needed to obtain values of the turbulent viscosity. There are several such equation sets that have been developed over the years to represent various turbulence models. The set selected here is the Shear Stress Transport (SST) model [57]. In general, the applicability of one or the other turbulence model has to be confirmed by information from experimentation. In this connection, the Shear Stress Transport (SST) model has received considerable support [58 – 61]. It represents a merging of two previously developed models, the k-ε and k-ω models. The quantity k is the turbulence kinetic energy, ε is the turbulence dissipation, and ω is the turbulent eddy frequency. The k-ε model has been demonstrated to give satisfactory descriptions ofy the velocity field at locations that are distant from bounding walls, and the k-ω model provides a good characterization of velocities in the near neighborhood of the wall.

A third set of equations was created to provide a means of dampening the turbulence kinetic energy predicted by the SST model [62, 63]. The dampening functions to diminish turbulence in the intermittent regime that is the transition between laminar and turbulent. A further functioning of the dampening is to suppress turbulence altogether in order to achieve purely laminar flow. The SST-

based dampening model is the only one that has been specifically adapted to internal flows.

The starting point of the analysis is the RANS generalization of the Navier-Stokes equations. These equations, as used here, are

$$\rho\left(u_i \frac{\partial u_j}{\partial x_i}\right) = -\frac{\partial p}{\partial x_i} + \frac{\partial}{\partial x_i}\left((\mu + \mu_{turb})\frac{\partial u_j}{\partial x_i}\right) \quad j = 1,2,3 \tag{4.2}$$

As written, these equations are applicable for incompressible flow with constant viscosity. These equations are augmented by the conservation of mass, which is

$$\frac{\partial u_i}{\partial x_i} = 0 \tag{4.3}$$

The Reynolds stresses are represented in Eq. (4.2) by the turbulent viscosity μ_{turb}.

The equations of the SST model are

$$\frac{\partial(\rho u_i \kappa)}{\partial x_i} = \gamma \cdot P_\kappa - \beta_1 \rho \kappa \omega + \frac{\partial}{\partial x_i}\left[\left(\mu + \frac{\mu_{turb}}{\sigma_\kappa}\right)\frac{\partial \kappa}{\partial x_i}\right] \tag{4.4}$$

$$\frac{\partial(\rho u_i \omega)}{\partial x_i} = A\rho S^2 - \beta_2 \rho \omega^2 + \frac{\partial}{\partial x_i}\left[\left(\mu + \frac{\mu_{turb}}{\sigma_\omega}\right)\frac{\partial \omega}{\partial x_i}\right] + 2(1 - F_1)\rho \frac{1}{\sigma_{\omega 2}\omega}\frac{\partial \kappa}{\partial x_i}\frac{\partial \omega}{\partial x_i} \tag{4.5}$$

The solution of Eqs. (4.4) and (4.5) yields the values of *k* and *ω*, which give the turbulent viscosity μ_{turb} from

$$\mu_{turb} = \frac{\alpha \rho \kappa}{\max(\alpha\omega, SF_2)} \tag{4.6}$$

Turbulence Dampening Model

$$\frac{\partial(\rho u_i \gamma)}{\partial x_i} = P_{\gamma,1} - E_{\gamma,1} + P_{\gamma,2} - E_{\gamma,2} + \frac{\partial}{\partial x_i}\left[\left(\mu + \frac{\mu_{turb}}{\sigma_\gamma}\right)\frac{\partial \gamma}{\partial x_i}\right] \tag{4.7}$$

and

$$\frac{\partial(\rho u_i \Pi)}{\partial x_i} = P_{\Pi,t} + \frac{\partial}{\partial x_i}\left[\sigma_{\Pi,t}(\mu + \mu_{turb})\frac{\partial \Pi}{\partial x_i}\right] \tag{4.8}$$

The nomenclature that appears in Eqs. (4.2) – (4.8) is:

A	model constant
$E_{\gamma 1}$, $E_{\gamma 2}$	intermittency destruction terms
F_1, F_2	blending functions in the SST model
P_k	production term for the turbulent kinetic energy
$P_{\gamma 1}$, $P_{\gamma 2}$	intermittency production terms
$P_{\Pi,t}$	production term for the transition onset Reynolds number
S	absolute value of the shear strain rate
u	local velocity
x_i	tensor coordinate direction
α	SST model constant
β_1, β_2	SST model constants
ω	turbulent eddy frequency
μ	molecular viscosity
μ_{turb}	turbulent viscosity
σ	Prandtl-number-like diffusion coefficient
γ	damping factor

ρ fluid density

Π turbulent adjunct function

It is relevant to discuss the manner in which the turbulence is damped. In that regard, reference may be made to Eq. (4.4), and, in particular, to the term involving P_k which represents the rate of production of turbulence kinetic energy. In the native form of Eq. (4.4), the multiplying factor γ does not appear. It is only when the total model of turbulence that includes intermittency and laminarization that γ is employed. It is, in fact, a damping factor which diminishes the rate of turbulence production.

These partial differential equations were discretized by means of finite-volume method. The discretization is performed within the software selected for effecting the solution. The chosen software package uses a unique solution algorithm. That algorithm can be characterized as the false-transient method.

To facilitate the discussion of that method, it is relevant to recall that any set of differential equations having time-independent boundary conditions will converge to a steady-state solution regardless of the initial conditions. A good example is the unsteady heat conduction equation. To solve that equation requires knowledge of ρ, c, and k. On the other hand, the solution to the steady-state conduction equation requires knowledge only of k. If the solution algorithm for attainment of steady-state results is phrased as a transient, then convenient false values of ρ and c can be assigned to accelerate the transient solution. The correct steady-state solution will be obtained regardless of the selected values of ρ and c. It has been demonstrated that for many types of problems, the false-transient approach will lead to a converged steady-state solution more rapidly than the more familiar iterative approach.

To obtain a steady-state solution for the three dimensional problem, a solution

domain was selected which encompassed the spaces through which fluid passed. That domain was bounded by solid walls except at the inlet and exit cross sections. The meshing of the solution domain is a critical activity. It was based on having high mesh densities in regions of high velocity gradients. Approximately five million nodes were employed. An accepted metric used to assess the sufficiency of a mesh is the value of y+ at wall-adjacent nodes. It is accepted in the numerical simulation community that a value of y+ of one is a characteristic of an excellent mesh. For the present calculations, the largest encountered value of y+ at the impingement surfaces of the collection modules was approximately 0.3. On this basis, it is believed that the mesh is satisfactory.

The specification of the boundary conditions is a critical aspect of the problem description. The solution was formulated as a mass-flow driven flow. This means that the mass flow rate was specified at the downstream end of the solution domain, from which the flow exited. The other bounding surfaces of the solution domain were specified as walls with the no-slip condition. Heat transfer was not included in any part of this model.

Convergence was monitored by one or two metrics. One of these was the attainment of residuals on the order of 10^{-6}. The other metric was to monitor the progression of the key results as the solution progressed with accumulating iterations. Convergence was indicated when these key results ceased to change over additional solution iterations.

RESULTS AND DISCUSSION

The results of this investigation encompass a broad range of significant information. Of immediate utility with regard to applications is the collection capability of the various zones that constitute the succession of targets. An understanding of this quantitative information rests upon knowledge of the patterns of fluid flow and the trajectories of the particles. The presentation of results will follow the sequence that has been described in the preceding sentences.

PARTICLE COLLECTION IN VARIOUS ZONES

The following table describes the percentage of each particle size captured in the various collection zones.

Table 4.1 – Particle capture in the various collection zones

	Collection Zones					
Particle Size	**First**	**Second**	**Third**	**Fourth**	**Fifth**	**TOTAL**
13 μm	100%	0%	0%	0%	0%	100%
8 μm	74%	26%	0%	0%	0%	100%
5 μm	1%	97%	2%	0%	0%	100%
3.1 μm	1%	36%	62%	0%	0%	100%
1.8 μm	0%	0%	0%	0%	0%	0%

Inspection of the table displays the distribution of capture for particles of different sizes. The largest among the particles, 13 μm, are very effectively captured in

the first zone. On the other hand, the 8-μm particles are distributed among zones one and two, with the lion's share being collected in the first zone. The third particle size, 5 μm, is very efficiently trapped in the second zone. The spread-mode of collection is in evidence for the fourth particle size, 3.1 μm. The fifth size, 1.8 μm, passed through the system without being collected in any zone.

The results conveyed in Table 4.1 provide clear evidence that the developed methodology is capable of determining where particles of difference sizes are deposited. This outcome warrants comparison with the original objective of the work. That goal was to develop a methodology for predicting the trajectories of therapeutic particulates ingested through the mouth or nose and passing through the respiratory system en route to targets in the lungs. The methodology had to be capable of dealing with a flow path of extraordinary complexity. It is believed that the modeled flow path (Figure 4.4) fulfills the complexity requirement. The displayed capability of the methodology to quantify the trajectories of the particles and to predict their zones of termination is clear testimony to the fulfillment of the enunciated goal.

FLUID FLOW PATTERNS

The solution domain used in these simulations contains a very complex network of abrupt changes of direction and highly variable flow-passage cross sections. Such intricate geometries often produce regions of steep pressure gradients and zones of flow separation. These features will give rise to non-uniform patterns of fluid flow throughout the system.

The presentation of fluid flow information begins with a focus on the inlet and the first collection zone, and Figure 4.8 has been prepared for this purpose. This figure is a color-contour diagram projected on a vertical plane cut through the center of the flow passage. The colors correspond to velocity magnitudes which are keyed to the legend at the upper left of the figure. The inlet section of the

flow path displays a variety of colors revealing regions of flow acceleration and flow separation. Owing to the convergence at the end of the inlet section, a high velocity, jet-like flow enters the first collection module. The jet impinges on the base of the collection zone and splashes radially outward. The spread is arrested by the vertical end walls, causing the flow to fold back on itself.

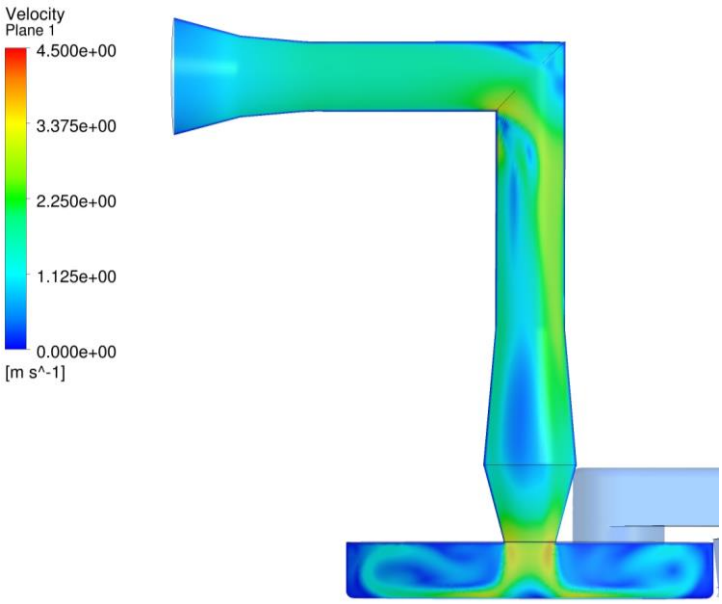

Figure 4.8 – Velocity contour diagram of inlet section and first collection zone

An alternative display of the fluid flow pattern in the initial portion of the system is by means of streamlines which are conveyed in Figure 4.9. The figure shows the convergence that spawns the strong jet at the lower end of the inlet section. The jet splash identified in the foregoing is readily observed. Note, however, that the jet splash and spread is not axisymmetric because the port through which the flow exits from the collection zone is situated unsymmetrically as can be seen in the figure. The streamlines converge at the exit port and pass into a bridge-like channel en route to the second collection zone.

Further examination of Figure 4.9 shows a non-symmetrical distribution of airflow streamlines through the assembly. A limited number of streamlines are shown in

the figure to preserve clarity. The walls of the solution domain are shown in a light blue color to assist in visualizing the geometry while still being able to see the streamlines within.

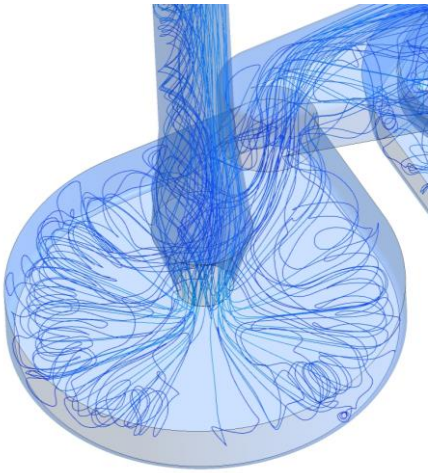

Figure 4.9 – Streamline pattern in the initial portion of the flow system

Further information about the flow pattern in the initial portion of the system can be obtained from Figure 4.10. This figure deals with the same portion of the system as was the focus of Figure 4.9 but the same space is viewed from a different vantage point. The main message of Figure 4.10 is the strong bias in the direction of jet spreading that is dictated by the location of the exit port.

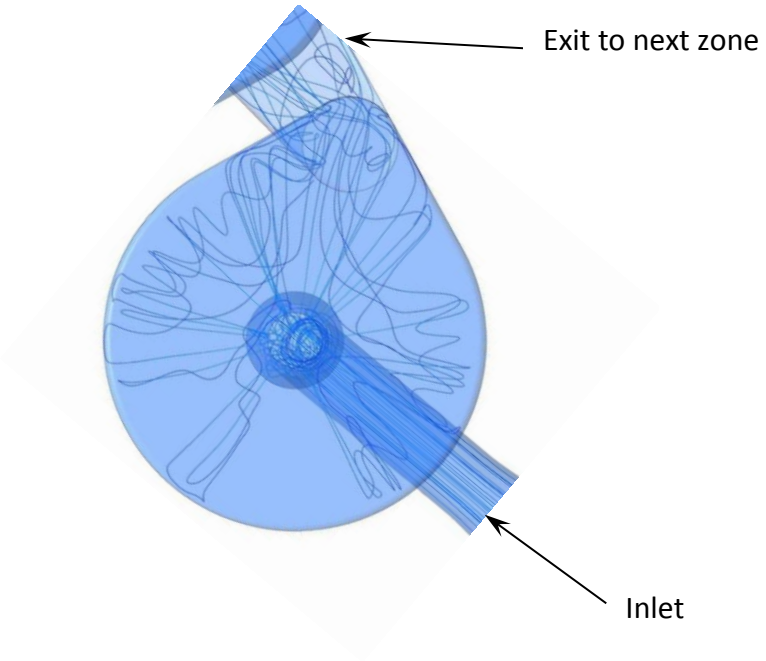

Figure 4.10 – Alternative view of the streamline pattern in the initial portion of the flow system

The nature of the flow through the passageways that interconnect the successive collection modules is illustrated in Figure 4.11. In particular, the pictured passageway interconnects the second and third modules. In addition, the figure shows the internal structure of the latter. The passage delivers the flow to the upper portion of the collection module. The delivered flow enters a plenum-like manifold. The bottom wall of the plenum is a perforated plate whose function is to spread the flow more or less uniformly as it enters the lower section of the collection module. The actual collection occurs at the lower surface of that section. Those particles that are not collected pass out of the zone and continue on to the next.

Close examination of the flow streamlines entering the collection zone reveals the presence of a swirl, or rotational component to the flow, demonstrating further

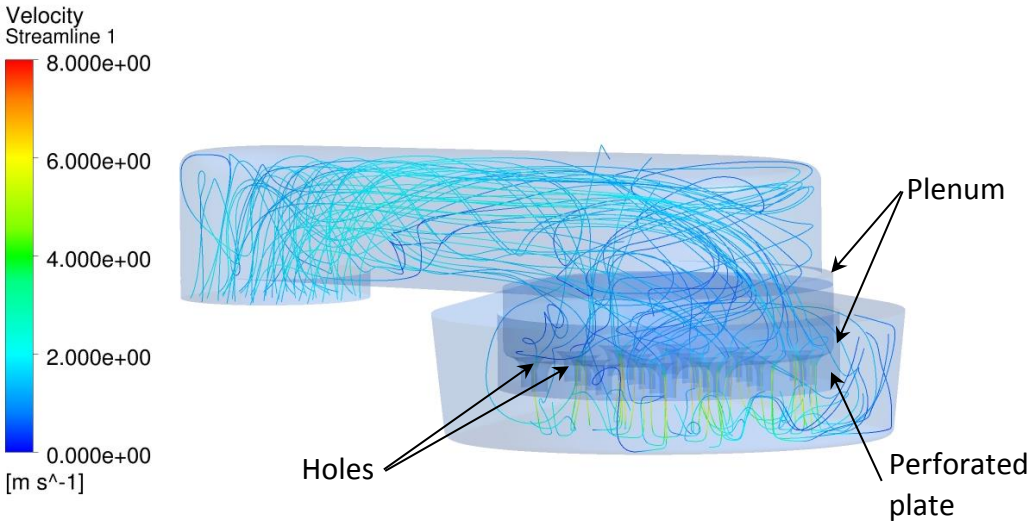

Figure 4.11 – View of the connecting passageway to the third collection zone and the internal structure of the module

complexity in the system. This swirl component can be seen by looking at the connecting passageways between any two collection modules in a manner similar to that of Figure 4.11.

More insights into the complexity of the flow system can be obtained by inspection of the internal structure of still another collection module, the fifth, which is shown in Figure 12. The direction of observation for the viewing of Figure 12 was chosen to reveal details that could not be easily seen in Figure 11. The flow is delivered to the plenum-type distribution manifold which constitutes the upper portion of the collection module. Clearly visible in the figure is the surface of the perforated plate which bounds the manifold from below. Of particular note is the very large number of holes which constitute the perforations. Clearly, by comparison of Figures 4.11 and 4.12, the number of perforation holes increases from one collection module to the next. Consequently, there is a concomitant increase of the complexity of the flow system geometry.

Figure 4.12 shows a closer view of the last collection module with a greater

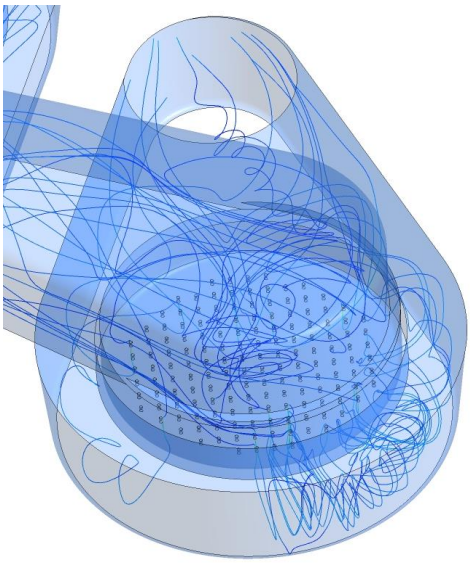

Figure 4.12 – Details of the fifth collection zone revealing flow system complexities

number of streamlines present. This figure makes the non-uniform velocity distribution more visible. It can be seen that the momentum carries the flow from the left side into the lower right portion (as viewed in the figure) of the collection zone, leaving a comparatively small amount of flow in the left section of the zone. The flow continues its bias as it progresses toward the exit port located at the top of the figure.

A vivid display of the flow produced by the multi-hole perforated plate of the fifth module is displayed in Figure 4.13, which is a velocity contour diagram that has been projected onto a vertical plane cut through the diameter of the plate. The jets created by the flow exiting the individual perforation holes are sharply etched. Although the jet velocities exiting the holes are as great as 20 m/s, there is a clear decrease of velocity with increasing distance from the exits.

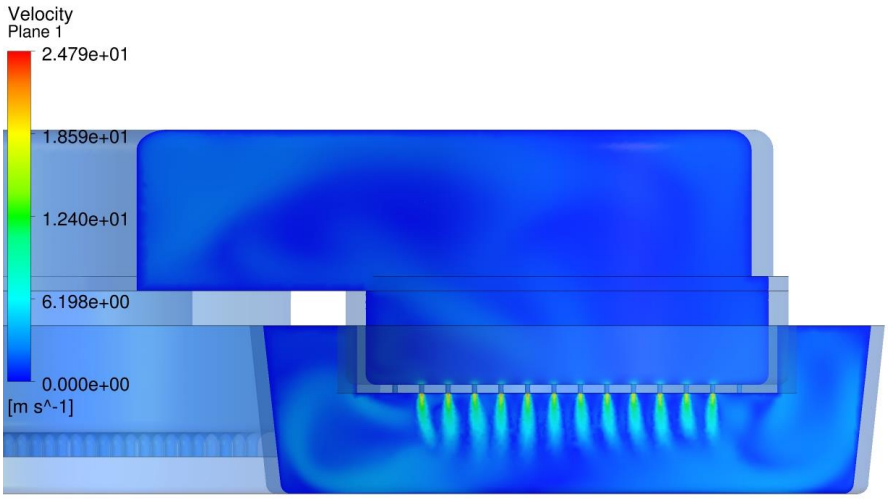

Figure 4.13 – Velocity contour diagram in a vertical plane cut through the perforated distribution plate of the fifth collection zone

Figure 4.14 is the final figure conveying the air flow patterns. The figure displays the streamlines which trace the air flow from its origins to its exit from the system. An overall appraisal of the figure is very convincing of both the small-scale and the large-scale geometric complexity experienced by the flowing air. This level of complexity is believed comparable to that of the actual respiratory system.

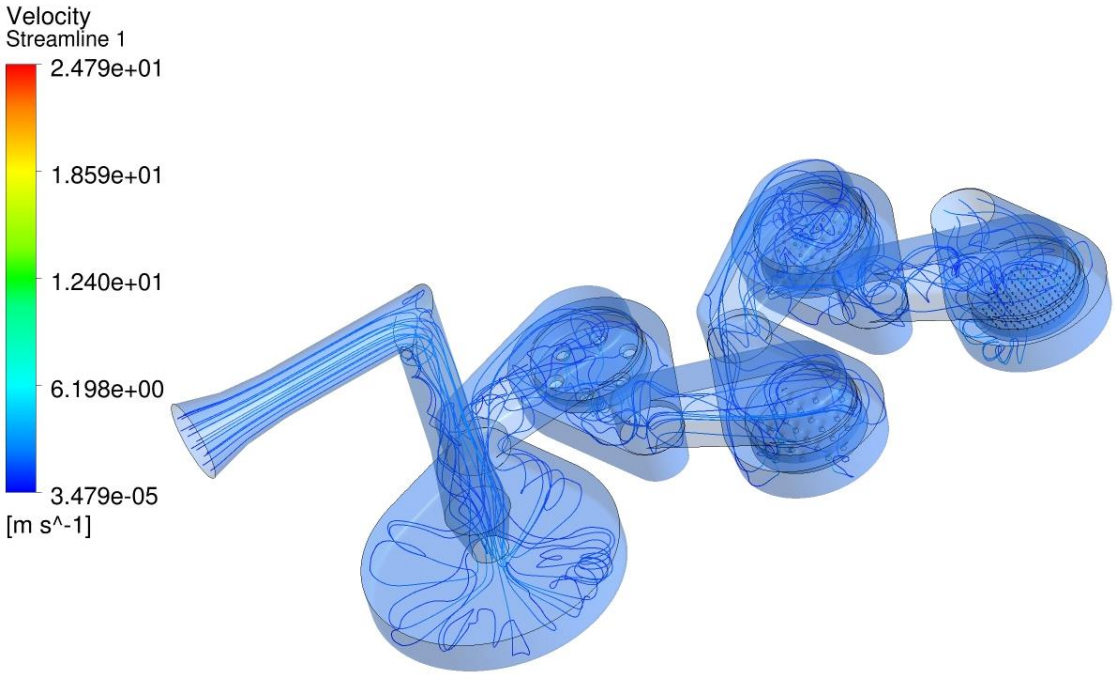

Figure 4.14 – Airflow streamlines through the entire system

PARTICLE MOTION

As previously discussed, particle impactors are designed to separate particles from a carrier fluid stream based on their relative sizes. The size of particle that will be collected in any particular collection zone will depend not only on the size and mass of the particle, but also on the flow pattern of the airflow in the specific zone and the distance from the exit of the jet to the bottom target surface. The first demonstration of particle motion is displayed in Figure 4.15. The figure shows the paths, indicated by lines of varying shades of blue, of 100 of the largest, 13-µm diameter, particles passing through the system. In this example, all of the particles impact the bottom of the first collection zone and are absorbed there. This

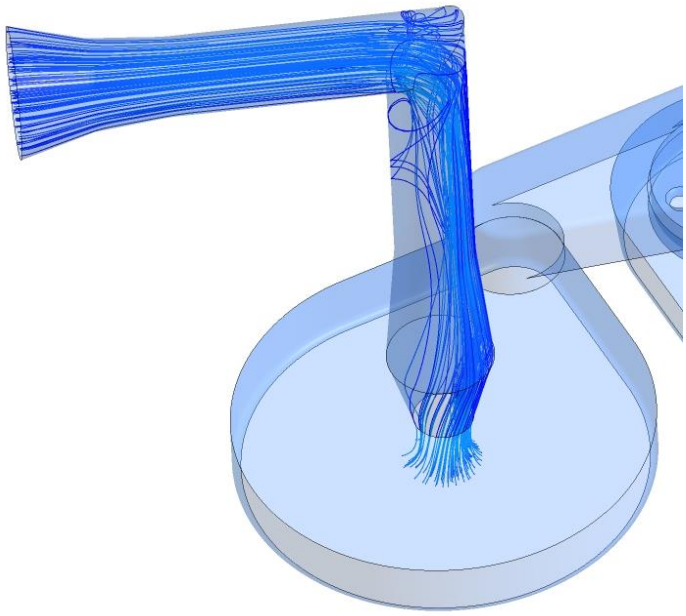

Figure 4.15 – Lines showing the paths of 13 µm particles all collecting in the first zone

termination is indicated in the figure by the blue lines coming to an end on the bottom surface of the zone, an outcome that was previously introduced in Table 4.1. Note that the paths of the particles seen in the figure are reminiscent of the previously exhibited streamlines of the airflow.

An alternative method of examining the spatial distribution of collected particles is shown in Figure 4.16. The figure illustrates the collection pattern of the 13-µm particles as they impacted the bottom surface of the first collection zone. The negative values shown in the legend to the left of the diagram are an indication of the positive direction of the coordinate system relative to the direction of the particles at time of impact. The deployment of the collected particles is not symmetric since the airflow is skewed as previously seen in Figures 4.9 and 4.10.

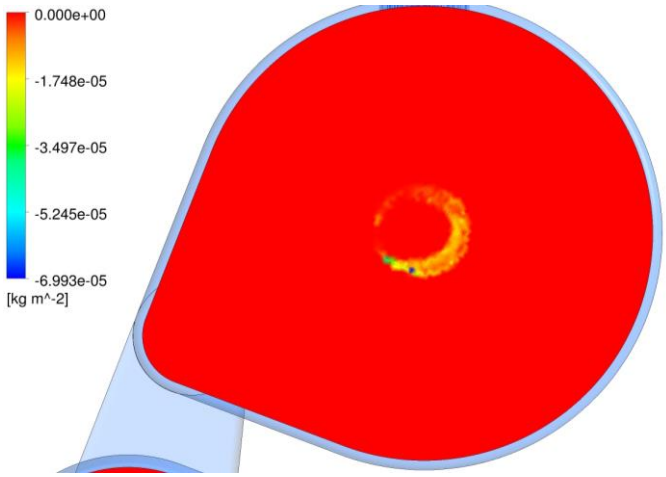

Figure 4.16 – A view from the bottom of the first collection zone showing the pattern of 13 µm particle deposition locations

Table 4.1 indicated that some of the 8-µm particles were collected in the first module as well as in the second module. Figure 4.17 is presented to illustrate a sample of the 8- µm particles that are respectively collected particles in these zones. The figure contains red circles to draw attention to some of the particles that were collected. Examination of the figure reveals that some of the particles stop in the first collection zone while many other particles can be seen leaving the first zone and continuing through the connecting passageway to the second collection zone. It can be seen that several particles stop in the second collection zone, and that there are not any 8-µm particles that leave the second zone.

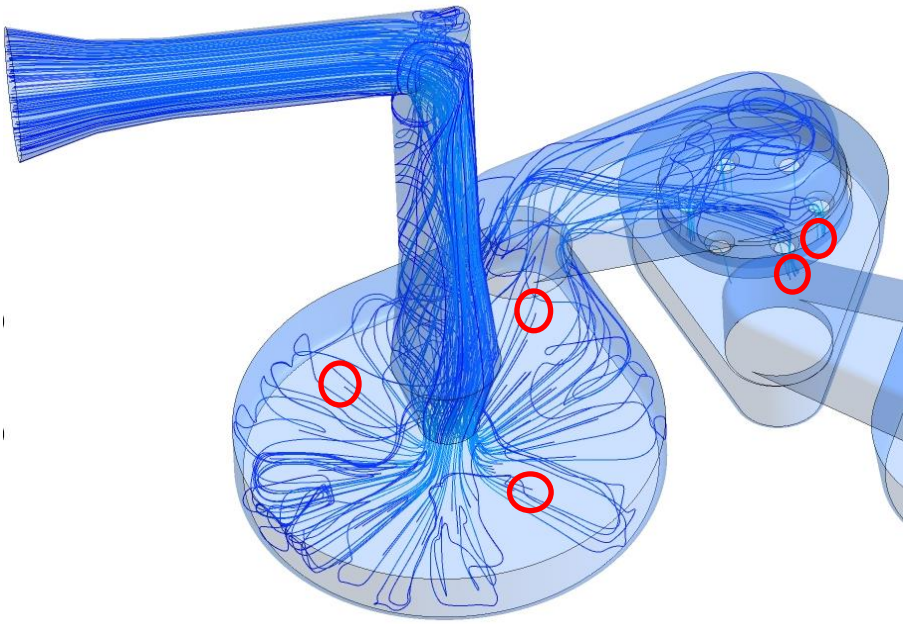

Figure 4.17 – Path of 8-µm particles through the first two collection zones. Red circles indicate particle(s) that stopped and were collected in the respective zone.

Figure 4.18 is presented to show, in a manner similar to Figure 4.16, where the 8-µm particles were collected on the bottoms of the first and second zones. It can be seen from Figure 4.18 that none of the 8 µm particles were collected in the third zone, which appears in the bottom of the figure. This agrees with the data in Table 4.1 which indicated that there were not any 8-µm particles collected in zones three, four, or five.

To supplement the results shown in Figs. 4.8-4.18, Table 4.2 is presented to provide additional quantitative data to describe the particle motion. The information shown in the table represents average travel time and distance for all like-sized particles. These tabulated results are in line with expectations. For

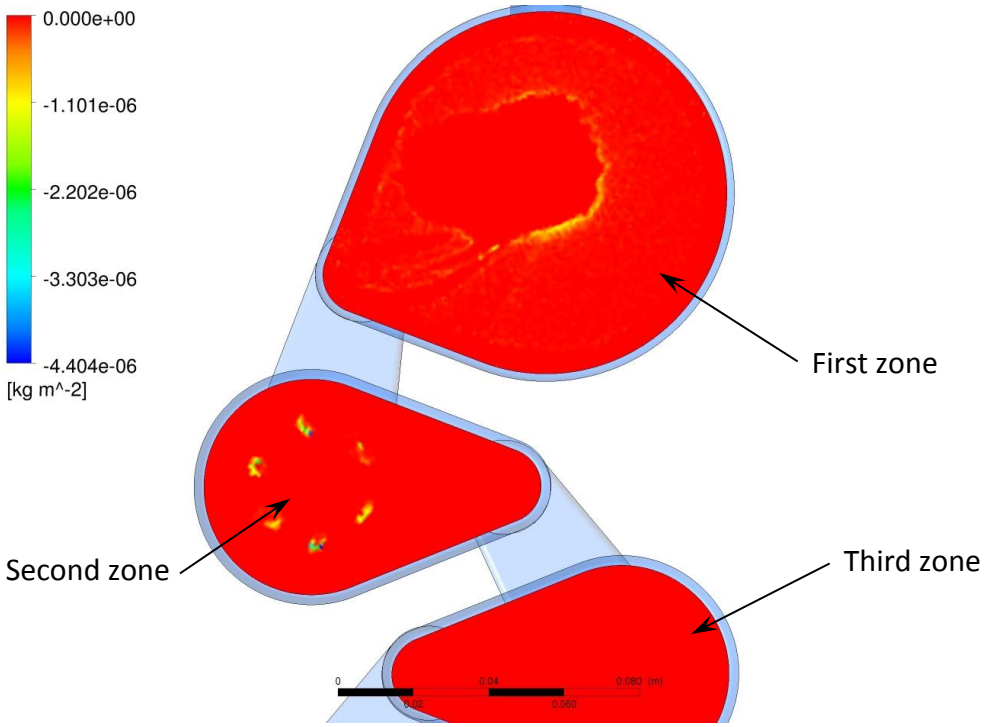

Figure 4.18 – View of the bottom of the first and second collection zones. The blue color represents the highest density of particles, followed by green, yellow and then orange.

example, Table 4.1 and Figure 4.15 indicated that all of the 13-µm particles were collected in the first zone, while all other particle sizes continued further into the system. It would be expected then, that these particles would have the shortest average traveling time and distance, as indicated in Table 4.2.

Table 4.2 – Average traveling distance and time for each particle size

Particle Size	Average Traveling Distance (cm)	Average Traveling Time (sec)
13 μm	14.0	0.092
8 μm	24.0	0.221
5 μm	36.7	0.321
3.1 μm	42.5	0.366
1.8 μm	44.0	0.361

CONCLUDING REMARKS

Medical treatment by means of inhalation of various nebulized drugs is a therapeutic modality being used to relieve patients of an increasing number of conditions. The drugs may take the form of small liquid droplets or particles and may be inhaled through the nose or the mouth. The efficacy of the treatment is highly dependent on the successful deposition of the drug at its intended target. The mechanism of drug delivery can be understood by study of particle transport theory.

Specifically, in this work, well-documented modalities in the field of particle impaction have served as guidance. Particle impaction theory dictates that when detailed knowledge of the carrier fluid motion is available, along with the size and mass of the particles of interest, it is possible to predict where the particles will be deposited with reasonable accuracy. Inertial impactors are a common and effective use of this technology in industry. In that instance, the fluid flow can be designed to give the specific characteristics that yield the desired separation of particles.

In the case of the human respiratory system, the fluid flow domain is not well defined or able to be specified. Additionally, it contains many features that create highly complex flows. These complexities make it increasingly difficult to accurately predict where particles might land and therefore produce challenges in achieving effective therapeutic results. Furthermore, particles of different size and mass will collect in different zones throughout the system. Owing to the fact that inhaled medications in the form of particles are often not necessarily of the same size, this reality produces further complications in getting the drug to the intended targets. Another significant variable presents itself since individual patients have different breathing patterns and speed of inhalation. These differences will significantly affect the fluid flow and particle trajectory and final landing location.

The work performed here demonstrates the capability and methodology that could be used to improve the design and efficacy of inhaled pharmaceuticals. The research of current literature revealed that models of the physical geometry of the human respiratory system can be obtained. It would be expected that this geometry would vary between patients, and this variability could be used as one element of a parametric study which would include particle size and mass, along with various air flow velocities and patterns. A series of CFD simulations could then be conducted which would optimize the particle size and mass with respect to the expected variability due to geometry and air flow velocities observed in a representative sample of patients. Benefits of such an approach could include higher treatment success rates, lower levels of ingested drugs required, reduced medication costs, and increased patient comfort and satisfaction.

CONCLUDING REMARKS

The work described herein discussed, in detail, several modalities of delivering therapeutic drugs to the human body utilizing a multiplicity of transport processes indigenous to mechanical engineering. Specifically, fluid mechanics and mass transfer formed the basis of a model to understand the delivery of a drug that is placed on a stent to reduce the rate of restenosis due to the patient's tissue rejecting the foreign device. The second investigated topic provided the fundamental underpinning for a novel non-surgical treatment option for menorrhagia by utilizing heat transfer, fluid mechanics, and phase change theory. The final chapter integrated fluid mechanic and particle transport theory to create a methodology for simulating the delivery of a pharmaceutical drug in particle form through the human respiratory system.

Atherosclerosis is a disease characterized by the buildup of plaque on the artery wall, thereby reducing the effective cross section of the lumen. This reduction of flow cross section creates additional pressure drop in the cardiovascular system and ultimately puts greater stress on the heart. Ultimately, portions of the plaque may break free and cause significant blockages downstream, resulting in a stroke or other more significant medical emergencies. A common treatment for this condition is to place a stent into the artery after an angioplasty to hold the artery walls in an open condition. It is found in many cases that after some time, the body rejects the stent and the tissue swells around the stent and creates another flow blockage. To help increase the probability of the body accepting the stent, it has become common to coat the stent with a drug which reduces inflammation in the artery walls. When the drug-coated stent is in place in the lumen, the drug can be transferred into the flowing blood by advection or into the artery walls via diffusion. Drug that transfers into the blood is carried away and is not useful in reducing any stent-induced inflammation of the artery walls. For this reason, it is important to understand and quantify what portion of the drug will diffuse into the tissue and what part is unavailable. This information can guide

the design of the stent and the amount of drug for a more effective result in the patient. The work described here provided a complete model to understand what portion of the drug transferred to the intended areas and what portion was lost into the flowing blood in the lumen. Further, the model was formulated in a universal fashion by transforming it into a dimensionless form. This form proves to be of great value as it allows for quick study of many different classes of problems with a single set of solutions.

Menorrhagia is a condition that affects a significant percent of the female population. The traditional remedies typically consisted of removal of all or part of the uterus. The quest for other less invasive treatments is easily understood and appreciated. A newly proposed treatment option having great promise utilizes condensing steam to provide adequate heat to achieve necrosis of the uterine lining. For this treatment to become an increasingly viable alternative, it is imperative to have a clear understanding of the effect of treatment duration on the depths and uniformity of tissue necrosis in the uterus. The created numerical simulation model auto-regulated the rate of vapor delivery to the uterine surface for subsequent condensation and thermal energy liberation. The model also included the most current understanding published in the literature of bioheat transfer as well as of the tissue damage integral. The results clearly showed close agreement with experimental results and highlighted the importance of calculating the tissue damage that occurs after termination of the application of steam; in particular, the necrosis depths found in the simulation also closely matched the non-uniform nature shown in the experimental results. The here-created simulation tools can now be used to further understand and develop a treatment modality that has significant advantages for the patient than more invasive options.

The utilization of medications which are administered by inhalation, either through the nose or mouth, is ever increasing. In many cases, the drug is presented in the form of small particles which are carried into the respiratory

system as the patient inhales. The effectiveness of the medication is influenced by obtaining the proper amount arriving at the targeted sites. The path that the particle-laden air flow must follow is of great complexity and gives rise to many opportunities for particles to be deposited in places other than the intended targets. It appears that there presently does not exist any predictions of air-carried particle trajectories through flow passages having complexities comparable to those encountered in the respiratory system.

This recognition motivated the third focus of this research. A model problem having flow-passage complexities comparable to those of the respiratory system was selected for the task of methodology development. The selected model problem is known to particle-technology practitioners and offers the advantage of known geometry.

The methodology developed here is built on concepts indigenous to particle transport theory and to particle capture by inertial impactors. The methodology was implemented by detailed numerical-simulation solutions of the model problem. The particle-laden airflow encompassed a range of particle sizes. The distribution of particle sizes in the several serially deployed collection zones demonstrated the target-reaching attributes of different sized particles.

The developed methodology could be used to track the trajectories and deposition sites of different size particles through various respiratory system geometries. A sensitivity analysis could be performed to quantify the amount of variability in particle deposition due to uncontrollable patient-specific factors. This capability could enable optimizing the drug particle size and mass based on the intended targets of the medication and lead to much more effective treatment for the patient with a reduction of the chances of complications, discomfort, and costs.

The work performed in this research illustrates how, with the ever-increasing capabilities of numerical simulation, biomedical therapies can be enhanced and

made more effective. By synergistic use of numerical simulation and clinical studies, new biomedical devices can be developed in shorter durations and subsequently be employed with a greater margin of safety.

REFERENCES

[1] V. Bush, The differential analyzer. A new machine for solving differential equations, Journal of the Franklin Institute 212 (4) (1931) 447–488.

[2] S. Zarek MD, H. Sharp MD, Global endometrial ablation devices, Clinical Obstetrics and gynecology 51(1) 2008 167-175.

[3] R. Mongrain, I. Faik, R. Leask, J. Rodés-Cabau, É. Larose, O. Bertrand, Effects of diffusion coefficients and struts apposition using numerical simulations for drug eluting coronary stents, J. Biomech. Eng. 129 (2007) 733-742.

[4] P. Zunino, C. D'Angelo, L. Petrini, C. Vergara, C. Capelli, F. Migliavacca, Numerical simulation of drug eluting coronary stents: Mechanics, fluid dynamics and drug release, Comput. Method. Appl. M. 198 (2009) 3633-3644.

[5] G. Vairo, M. Cioffi, R. Cottone, G. Dubini, F. Migliavacca, Drug release from coronary eluting stents: A multidomain approach, J. Biomech. 43 (2010) 1580-1589.

[6] C. Hwang, D. Wu, E. Edelman, Physiology transport forces govern drug distribution for stent-based delivery, Circulation (2001) 600-605.

[7] G. Pontrelli, F. de Monte, Modeling of mass dynamics in arterial drug-eluting stents, J. Porous Media 12(1) (2008) 19-28.

[8] G. Pontrelli, F. de Monte, Mass diffusion through two-layer porous media: an application to the drug-eluting stent, Int. J. Heat Mass. Tran. 50 (2007) 3658-3669.

[9] P. Zunino, Multidimensional pharmacokinetic models applied to the design of drug-eluting stents, Cardiovasc. Eng. 4(2) (2004) 181-191.

[10] M. Grassi, G. Pontrelli, L. Teresi, G. Grassi, L. Comel, A. Ferluga, L. Galasso, Novel design of drug delivery in stented arteries: A numerical comparative study, Math. Biosci. Eng. 6(3) (2009) 493-508.

[11] G. Pontrelli, F. de Monte, A multi-layer porous wall model for coronary drug-eluting stents, Int. J. Heat Mass Transf. 53 (2010) 3629-3637.

[12] B. O'Connel, M. Walsh, Demonstrating the influence of compression on artery wall mass transport, Ann. of Biomed. Eng. 38 (4) (2010) 1354-1366.

[13] B. O'Connel, T. McGloughlin, M. Walsh, Factors that affect mass transport from drug eluting stents into the artery wall, Biomed. Eng. Online (2010) 9:15.

[14] D. Sakharov, L. Kalachev, D. Rijken, Numerical simulation of local pharmacokinetics of a drug after intravascular delivery with an eluting stent, J. Drug Target. 10 (6) (2002) 507-513.

[15] C. Vergara, P. Zunino, Multiscale boundary conditions for drug release from cardiovascular stents, Multiscale Model. Sim. 7(2) (2008) 565-588.

[16] S. Rugonyi, Effect of blood flow on near-the-wall mass transport of drugs and other bioactive agents: A simple formula to estimate boundary layer concentrations, J. Biomech. Eng. 130 (2008) 021010-1 – 021010-7.

[17] Wikipedia, http://en.wikipedia.org/wiki/Menorrhagia, 2013.

[18] D. Hill, P. Maher, Intrauterine surgery using electrocautery, Australian and New Zealand Journal of Obstetrics and Gynaecology 30 (2) (1990) 145-146.

[19] H. T. Sharp, Assessment of new technology in the treatment of idiopathic menorrhagia and uterine leiomyomata, Obstetrics and Gynecology 108 (4) (2006) 990-1003.

[20] Lipscomb, G, Glob. libr. women's med., (ISSN: 1756-2228) 2008; DOI 10.3843/GLOWM.10024.

[21] S. M. van der Kooij, W. M. Ankum, W. J. K. Hehenkamp, Review of nonsurgical/minimally invasive treatments for uterine fibroids, Curr Opin Obstet Gynecol 24 (6) 2012 368-375.

[22] S. Yeasmin, K. Nakayama, M. Ishibashi, A. Katagiri, K. Iida, N. Nakayama, S. Aoki, Y. Kanaoka, K. Miyazaki, Microwave endometrial ablation as an alternative to hysterectomy for the emergent control of uterine bleeding in patients who are poor surgical candidates, Gynecology and obstetrics, 280 (2) 2009 279-282.

[23] B. Feldberg, N. J. Cronin, A 9.2 GHz microwave applicator for the treatment of menorrhagia, IEEE MTT-S Digest (1998) 755-758.

[24] E. Downes, R. Yasmin, R. Flemming, Microwave endometrial ablation: Development and clinical application, Surgical Technology International, 16 (2007) 142-146.

[25] Hong WK. American Association for Cancer Research. Cancer Medicine, 8th Ed. Shelton, Conn.: People's Medical Pub. House; 2010.

[26] Dewhirst MW, Viglianti BL, Lora-Michiels M, Hanson M, Hoopes PJ. Basic principles of thermal dosimetry and thermal thresholds for tissue damage from hyperthermia. Int J Hyperthermia 19 (3) (2003) 267-294.

[27] Pearce JA, Thomsen S. Kinetic models of laser-tissue fusion processes. Biomed Sci Instrum 29 (1993) 355-360.

[28] McMurray T, Pearce JA. Thermal damage quantification utilizing tissue birefringence color image analysis. Biomed Sci Instrum 29 (1993) 235-242.

[29] Dewhirst MW, Lora-Michiels M, Viglianti BL, Dewey WC, Repacholi M. Carcinogenic effects of hyperthermia. Int J Hyperthermia 19 (3) (2003) 236-251.

[30] Yarmolenko PS, Moon EJ, Landon C, Manzoor A, Hochman DW, Viglianti BL, Dewhirst MW. Thresholds for thermal damage to normal tissues: an update. Int J Hyperthermia 27 (4) (2011) 320-343.

[31] Sapareto SA, Dewey WC. Thermal dose determination in cancer therapy. International journal of radiation oncology, biology, physics 10 (6) (1984) 787-800.

[32] Lepock JR. Cellular effects of hyperthermia: relevance to the minimum dose for thermal damage. International Journal Of Hyperthermia 19 (3) (2003) 252-266.

[33] K. Diller, J. Valvano, J. Pearce, (2000). Bioheat Transfer. In: F. Kreith (Ed.) *CRC Handbook of Thermal Engineering* (4-114 – 4-188). Boca Raton: CRC Press LLC.

[34] Arrhenius S. Uber die Reaktionsgeschwindigkeit bei der Inversion von Rohrzucker durch Sauren (On the Reaction Rate in the Inversion of Cane Sugar by Acids). Z Phys Chem 4 (1889) 226-248.

[35] Arrhenius S. Quantitative Laws in Biological Chemistry. London: G. Bell & Sons; 1915. 184 p.

[36] Johnson FH, Eyring H, Stover BJ. The Theory of Rate Processes In Biology and Medicine. New York: John Wiley & Sons; 1974.

[37] Eyring H. The Energy of Activation for Bimolecular Reactions Involving Hydrogen and the Halogens, According to Quantum Mechanics. Journal of the American Chemical Society, 53 (1931) 2537-2549.

[38] Eyring H. The Activated Complex in Chemical Reactions. Journal of Chemical Physics 3 (2) (1935) 107-115.

[39] Eyring H, Polyani M. Über Einfache Gasreaktionen (On Simple Gas Reactions). Zeitschrift fur Physikalische Chemie B 12 (1931) 279-311.

[40] Polyani M. Atomic Reactions. London: Williams - Norgate; 1932.

[41] J. A. Pearce, Relationship between Arrhenius models of thermal damage and the CEM 43 thermal dose. Energy-based Treatment of Tissue and Assessment V. Volume 7181. San Jose, CA, United States: SPIE, P.O. Box 10, Bellingham WA, WA 98227-0010, United States; 2009. p 718104-718101-718104-718115.

[42] J. Olsrud, B. Friberg, M. Ahlgren, B. R. R. Persson, Thermal conductivity of uterine tissue in vitro, Phys. Med. Biol., 43 (1998) 2397-2406.

[43] IT'IS Foundation website, http://www.itis.ethz.ch/itis-for-health/tissue-properties/database/thermal-conductivity/.

[44] Balasubramaniam, T. A., H. F. Bowman, Thermal conductivity and thermal diffusivity of biomaterials: A simultaneous measurement technique, J. Biomech. Engr. 99 (1977) 148-154.

[45] M. L. Cohen, Measurement of the thermal properties of human skin, A review, J. Invest. Dermatol, 69 (1977) 333-338.

[46] H. Pennes, Analysis of tissue and arterial blood temperatures in the resting human forearm, J. Appl. Physiol. 85 (1948) 5-34.

[47] J. P. Abraham, E. M. Sparrow, A thermal-ablation bioheat model including liquid-to-vapor phase change, pressure- and necrosis-dependent perfusion, and moisture-dependent properties, Int. J. Heat Mass Transf. 50 (2007) 2537-2544.

[48] Personal communication, Aegea Medical, 1/13/13.

[49] K. Chin, N. Mulchan, S. Hong, S. Yoon, BEE 4530, Computer aided engineering: Applications to biomedical processes, Final report.

[50] P. W. Longest, M. Hindle, S. D. Choudhuri, Effects of generation time on spray aerosol transport and deposition in models of the mouth-throat geometry, Journal of aerosol medicine and pulmonary drug delivery, 22 (2) (2009) 67-83.

[51] J. Sandeau, I. Katz, R. Fodil, B. Louis, G. Apiou-Sbirlea, G. Caillibotte, D. Isabey, CFD simulation of particle deposition in a reconstructed human oral extrathoracic airway for air and helium-oxygen mixtures, Journal of aerosol science, 41 (2010) 281-294.

[52] C-L. Lin, M. H. Tawhai, E. A. Hoffman, Multiscale image-based modeling and simulation of gas flow and particle transport in the human lungs, WIREs Syst Biol Med 2013, 5:643–655. doi: 10.1002/wsbm. 1234.

[53] P. Roth, C. F. Lange, W. H. Finlay, The effect of breathing pattern on nebulizer drug delivery, Journal of aerosol medicine, 16 (3) (2003) 325-329.

[54] J. Heyder, M. Svartengren, (2002). Basic Principles of particle behavior in the human respiratory tract. In: H. Bisgaard, C. O'Callaghan, G. Smaldone (Eds.) *Drug delivery to the lung* (21-45). New York: Marcel Dekker.

[55] V. A. Marple, K. Willeke, (1976). Inertial impactors: Theory, design and use. In Y. H. Liu (Ed.) *Fine Particles, Aerosol Generation, Measurement, Sampling, and Analysis* (411-446). Academic Press, Inc.

[56] C. J. Reagle, J. M. Delimont, W. F. Ng, S. V. Ekkad, V. P. Rajendran, Measuring the coefficient of restitution of high speed microparticle impacts using a PTV and CFD hybrid technique, Measurement science and technology, 24 (2013) 1-11.

[57] F. Menter, Two-equation eddy-viscosity turbulence models for engineering applications, AIAA J 30 (1994) 1598-1605.

[58] E. Sparrow, J. Gorman, J. Abraham, Quantitative assessment of the overall heat transfer coefficient U, Journal of heat transfer, 135 (2013) 61102-1 – 61102-7.

[59] J. Abraham, E. Sparrow, J. Tong, Heat transfer in all pipe flow regimes: laminar, transitional/intermittent, and turbulent, International Journal of Heat and Mass Transfer, 52 (2009) 557-563.

[60] J. Stark, J. Gorman, M. Hennessey, F. Reseghetti, J. Willis, J. Lyman, J. Abraham, M. Borghini, A computational method for determining XBT depths, Ocean Science, 7 (2011) 733-743.

[61] J. Abraham, J. Gorman, F. Reseghetti, E. Sparrow, W. Minkowycz, Drag coefficients for rotating expendable bathythermographs and the impact of

launch parameters on depth predictions, Numerical Heat Transfer, Part A, 62 (2012) 25-43.

[62] F. Menter R.B. Langtry, S.R. Likki, Y.B. Suzen, P.G. Huang, S. Volker, A correlation-based transition model using local variables – part 1: model formulation, J. Turbomachinery 129 (2006) 413-422.

[63] R.B. Langtry, F. Menter, S.R. Likki, Y.B.Suzen, P.G. Huang, S. Volker, A correlation-based transition model using local variables – part 2: test cases and industrial applications, J. Turbomachinery 128 (2006) 423-434.